

NuSTAR view of Swift/BAT AGN: The R - Γ correlation [★]

C. Panagiotou and R. Walter

Astronomy Department, University of Geneva, Chemin d'Ecogia 16, 1290 Versoix, Switzerland
e-mail: Christos.Panagiotou@unige.ch

Received ***; accepted ***

ABSTRACT

Context. The reflection hump is a prominent feature in the hard X-ray spectrum of active galactic nuclei (AGN). Its exact shape and its correlation to other quantities provide valuable information about the inner and outer regions of an AGN.

Aims. Our main goal is to study the reflection hump in a large sample of nearby AGN. We aim to investigate the evolution of reflection with absorption and its correlation with the spectral index.

Methods. We analysed archived *NuSTAR* observations of the 70-month BAT catalogue AGN. By performing a detailed spectral analysis, we were able to constrain the spectral parameters and to investigate the reflection emission in a large sample of individual sources.

Results. The reflection strength was found to be strongly correlated with the power-law slope in unabsorbed sources, pointing towards disc reflection for these sources. Different possible explanations were tested and the most likely one is that the corona is moving either towards or away from the disc with a moderately relativistic velocity. An $R - \Gamma$ correlation was not detected for absorbed sources. In addition, these AGN feature harder spectra, suggesting intrinsic differences between the two classes or a slab geometry for the X-ray source.

1. Introduction

The X-ray emission of Active Galactic Nuclei (AGN) is thought to originate from a compact region located close to the central supermassive black hole. According to the currently accepted model, UV and optical photons emitted by the accretion disc enter a region filled with high-energy electrons, often referred to as corona, and are upscattered to X-rays by inverse Compton scattering. Part of this primary X-ray emission is then intercepted by the surrounding material and reflected towards our line of sight.

The spectrum of thermal Comptonisation in an optically thin region is approximately represented by a cut-off power law, which has been found to aptly describe the observed X-ray spectra of AGN (e.g. Haardt & Maraschi 1993). In addition, a distinct reflection feature is commonly observed. The so-called Compton hump is an excess of emission in comparison to a simple power-law peaking at ~ 30 keV. Finally, a fluorescent iron line at ~ 6.4 keV is prominent in the spectra of most AGN. This line is also produced by the interaction of the primary X-ray emission with the surrounding material.

According to the unification model of AGN (Antonucci 1993), a toroidal dusty region surrounds both the corona and disc structure. The so-called torus was initially proposed to account for the lack of broad emission lines in the optical spectrum of Type 2 AGN. If it lies in our line of sight, the gas in the torus will also absorb part of the X-ray emission. In addition to producing absorption effects, the torus is expected to contribute significantly to the reflected emission, together with the disc.

Although the above model is successful in explaining the broad characteristics of AGN X-ray emission, there are still many open questions that require more careful treatment. Several works have followed different techniques with the aim of

improving our understanding of the central X-ray source and its surrounding geometry.

Time variability and microlensing studies (e.g. Mosquera et al. 2013) have been successful in constraining the X-ray source position within a few tens of gravitational radii from the black hole. More recently, the development of reverberation techniques allowed to study the regions in the immediate vicinity of the black hole. These studies have put stronger constraints on the position of the corona with respect to the black hole and have also identified the inner disc as the main source of the Fe line and Compton hump emissions for a handful of sources (e.g. Zoghbi et al. 2014; Kara et al. 2015).

Another commonly followed approach to study the AGN X-ray emission is the investigation for correlation amongst the various spectral parameters or physical parameters. Such correlations are expected to be driven by the underlying physical processes or the exact geometry of the source and could, therefore, provide additional information.

Brightman et al. (2013) have found that the power-law slope is positively correlated to the Eddington ratio, suggesting that the accretion rate determines the physical conditions of the corona. The situation is more complicated when the dependence of the slope on the X-ray luminosity is explored. Some studies (e.g. Saez et al. 2008) have suggested the existence of a positive correlation, while others (e.g. Scott et al. 2011) observed the opposite trend. On the other hand, studies based on a local sample have found no evidence of a significant correlation (e.g. Winter et al. 2009).

The reflection strength, R , which is a parametrisation of how strong the reflected emission is with respect to the primary power-law, was also found to be correlated to the X-ray slope. Zdziarski et al. (1999) were the first to observe a positive correlation between the two parameters for a group of Seyfert galaxies, which they interpreted as a result of the interplay between the disc and the corona. Although the robustness of this correlation was questioned by Vaughan & Edelson (2001), Zdziarski et al.

[★] Full Tables 4, 5, and 6 are available in electronic form at the CDS via anonymous ftp to cdsarc.u-strasbg.fr (130.79.128.5) or via <http://cdsweb.u-strasbg.fr/cgi-bin/qcat?J/A+A/>.

(2003) studied in detail the various systematic and statistical effects and confirmed the reality of the above correlation. More recently, Zappacosta et al. (2018) found an anti-correlation between R and the X-ray luminosity.

In Panagiotou & Walter (2019), we studied the X-ray properties of a sample of nearby Seyfert galaxies using the Nuclear Spectroscopic Telescope Array (NuSTAR, Harrison et al. 2013), the first telescope focusing X-rays above 10 keV, which makes it ideal to study the reflection hump in individual AGN. We found that the reflection emission varies with absorption, which potentially points to a different origin of reflection between absorbed and unabsorbed sources. Reflection was found to correlate with the X-ray slope in unabsorbed sources, while evidence for a correlation between the observed absorption and the reflection was found for the obscured sources.

Motivated by these results, we expanded our analysis to a much larger sample. Our main goal was to study the hard X-ray spectrum of AGN and investigate for differences between absorbed and unabsorbed sources. In this work, we present the analysis of non Compton thick sources, focusing mainly in the observed R - Γ correlation and its interpretation. We describe the considered sample and the applied reduction in Sect. 2. The spectral analysis followed in this study is discussed in Sect. 3. The results are presented in Sect. 4 and are discussed in further detail in Sect. 5. Our main findings are summarised in Sect. 6.

2. Data sample and reduction

Our sample comprises the sources of the 70-month Swift-BAT catalogue (Baumgartner et al. 2013) that were observed by NuSTAR and which had public archival data until April 2019. We considered the sources that are categorised as Class 4 and 5 in the BAT catalogue, which correspond to the Type 1 and 2 Seyfert galaxies, respectively. In total, there were 128 Seyfert 1 and 168 Seyfert 2 objects.

We followed the standardised procedure in order to reduce the observational data. We used the NuSTAR Data Analysis Software (NuSTARDAS) package to produce clean event files. Due to the passage of NuSTAR through the South Atlantic Anomaly (SAA) area, some events were removed when needed. The source spectra were extracted from a circular region centered on the source's celestial coordinates and the background spectra from a source-free annulus surrounding the source region. When the source was located close to the detector's edge or close to another source, the background spectrum was extracted from a nearby source-free circular region. The source region's radius was determined by a visual examination of the source's image with the aim to maximise the signal-to-noise ratio, while the inner radius of the background annulus was always defined to be at least 30 arcseconds larger than the source's radius in order to avoid source contamination. Finally, all the source spectra were binned with at least 25 source counts per bin.

We, then, examined the spectral variability of all sources with more than one observation. When the source spectral shape was found to be not significantly variable, we calculated its average spectrum using the *addspec* tool. A spectral variability is considered as non-significant when an initial fit of the different observations reveals that the spectral parameters are consistent within the errors between the observations, with a potential exception for the normalisation. In other words, we estimated an average spectrum when the spectral shape of the source remains the same, while its flux state might be variable. If the source spectrum was moderately variable, we considered the spectrum of each individual observation separately. Finally, there were a

few sources that underwent severe variability between their observations, showing a transition from a reflection dominated to a continuum dominated spectrum. These sources were omitted from the subsequent analysis.

Several more sources were excluded based on various criteria. First, we excluded the sources with a low signal-to-noise ratio. Only the sources with $S/N > 31$ ¹, which was found to be sufficiently high for the spectral parameters to be constrained, were considered in this study. Second, we excluded the sources featuring a reflection dominated spectrum. Initially, we pursued a model-independent approach, calculating the following softness ratio:

$$SR = \frac{CR_{3-5} - CR_{25-35}}{CR_{3-5} + CR_{25-35}}, \quad (1)$$

where CR_{3-5} denotes the count rate from 3 to 5 keV and CR_{25-35} the count rate from 25 to 35 keV. We have found that the sources with $SR < 0.2$ have a reflection dominated spectrum and are more likely to be Compton thick (Panagiotou & Walter 2019, where all sources categorised as Class 5 have $SR < 0.2$). Therefore, we decided to exclude the sources with $SR < 0.2$ from our current analysis. It should be noted that using a different energy range for the hard X-rays (say 15-25 keV) does not modify our results. In addition, we excluded some sources for which the spectral model discussed in Sect. 3 required a large amount of reflection (reflection parameter $R > 4$) to be well fitted. All these sources, with an apparent reflection dominated spectrum, require a complex spectral model.

We also excluded the galaxies that have been found to host a LINER, as well as *SWIFT J0319.7+4132*, which lies in the center of Perseus cluster. All the sources that have been excluded are listed in Table 3.

After the exclusion of sources, the considered sample consists of 113 Seyfert 1 and 101 Seyfert 2. Nearly a fourth of them (24 Seyfert 1 and 27 Seyfert 2) have already been studied in Panagiotou & Walter (2019), where we retrieved the results from. For the new sources, we followed the spectral analysis outlined in the next section. This analysis and the corresponding assumptions are the same as these followed in Panagiotou & Walter (2019). The objects' characteristics and their observational details are listed in Tables 4 and 5, respectively. The sources denoted by a dagger in the former table have been analysed in Panagiotou & Walter (2019).

The used sample spans a range of luminosities and redshifts. Figure 1 plots the distribution of redshift and BAT 14-195 keV observed luminosity.

3. Spectral Analysis

3.1. Baseline model

The spectra of all sources were fitted by the same model. The spectra of the two NuSTAR detectors, FPMA and FPMB, were considered together allowing for a cross-normalisation constant to be minimised. The XSPEC software (Arnaud 1996) was used for the fitting procedure and the element abundances of Asplund et al. (2009) were assumed. We performed the model fitting using χ^2 statistics. All the errors reported in this work correspond to 1- σ confidence interval, unless otherwise noted. We have assumed a Λ CDM cosmology of $H_0 = 70 \text{ km/s/Mpc}$ and $\Omega_\Lambda = 0.73$.

¹ The signal-to-noise ratio is calculated using the spectrum of both detectors FPMA and FPMB.

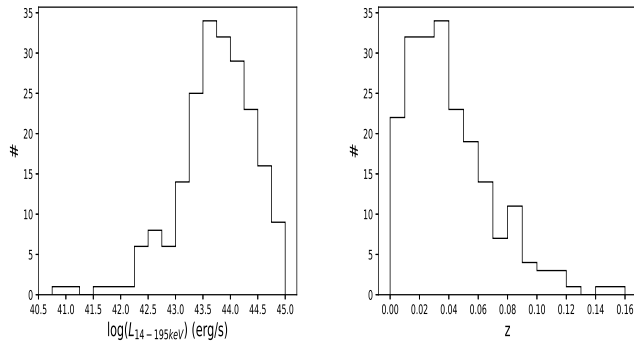


Fig. 1: Distribution of the 14-195 keV luminosity (left) and redshift (right panel) of the used sources, as given in the BAT catalogue.

We used the phenomenological model *pexrav* (Magdziarz & Zdziarski 1995) to simulate the AGN emission as a power-law with an exponential cut-off at high energies plus a reflection component produced by the scattering of the power-law emission in a neutral medium with an infinite optical depth. This emission is modified by photoelectric absorption, modelled by *zphabs* in XSPEC, due to the existence of gas in the host galaxy. The absorption due to the Galactic interstellar medium was not considered. Towards most of the sources the Galactic absorption column density is well below 10^{22} cm^{-2} , and thus has an insignificant effect on the NuSTAR spectra, which start at 3 keV, even for *SWIFT J1347.4-6033* and *J2018.8+4041*, for which $N_{H, \text{Gal}} = 0.96$ and $1.1 \cdot 10^{22} \text{ cm}^{-2}$, respectively.

Finally, we used a gaussian emission line centered at 6.4 keV, to account for the Fe $K\alpha$ line. To simplify the fit we assumed the existence of only one narrow Fe line, with a width fixed at 0.05 keV, unless it was otherwise needed by the fit (Sect. 3.2). We, furthermore, assumed the same inclination angle for all the sources, $\cos i = 0.45$, and solar abundances for the reflecting and absorbing media. There were seven model parameters left to be minimised during the fit, that is the intrinsic absorption column density, N_H , the power-law index, Γ , the reflection strength, R , the energy of the cut-off, E_C , the two normalisations of the iron line and of the power-law and the cross-normalisation between the two detectors.

The above model was initially used to fit all the observed spectra and provided a statistically accepted fit for the majority of the sources. There were several sources, for which a more careful treatment of the Fe emission was needed. These objects are discussed in detail in Sect. 3.2. In addition, seven sources with multiple observations were found to exhibit a moderate spectral variability between the observation periods. We fitted the individual spectra of each observation for these objects. These sources have been excluded from the subsequent analysis of the different classes (Sect. 3.3).

Furthermore, the best-fit Γ for thirteen sources was found to be below 1.4. Such a small value is unphysical and not commonly observed in the spectra of AGN. These small values might be an artifact of the fit. The spectral shape of a highly absorbed source might be equally well reproduced by a less absorbed low- Γ power-law with a small energy cut-off and by an absorbed power-law of larger Γ , E_C and R . Therefore, we fixed Γ to a value of 1.73² and repeated the fit for these sources. The new fits are

² This is the average best-fit Γ of the MOB class (Sect. 3.3), to which all these sources belong.

still statistically accepted. Although we give the results for these sources, we excluded them from the subsequent discussion to avoid introducing biases in our results.

Table 6 lists the best-fit results for all sources. The last column provides an indication of the goodness of fit, listing the best-fit χ^2 statistic and the corresponding degrees of freedom. The fit was overall good for all the sources, with the mean reduced χ^2 of all the fits being $\chi^2_{\nu} = 0.99$.

3.2. Fe $K\alpha$ line

A detailed study of the iron's line spectral shape in the individual sources is outside the scope of this work. Therefore, we decided to fix the line width at 0.05 keV. There are several sources, however, for which the fit is significantly better when the width is left free to be minimised and the best-fit width is found to be larger than 0.05 keV even at a $3 - \sigma$ level. We examined the fit's residuals when a narrow line is assumed for each of these sources and modified the fit as follows.

Following Ursini et al. (2015), we included three gaussian emission lines in our model for *SWIFT J2209.4-4711*, all assumed to be narrow. The lines, which are centered at 6.4, 6.7, and 6.966 keV, model the emission from neutral Fe, Fe XXV, and Fe XXVI, respectively. The model with three lines provided an improved fit with $\Delta\chi^2 = 51$ in comparison to the model with only one narrow line.

The spectral fit of *SWIFT J2304.8-0843* revealed the existence of a second emission line in its spectrum. Adding a second narrow line improved the fit by $\Delta\chi^2 = 17$ and the line was found to be centered at $E = 6.93^{+0.08}_{-0.07}$ keV. The inclusion of a second line improved the fit significantly ($\Delta\chi^2 = 24$) for *SWIFT J0433.0+0521*, as well. The existence of a line at $E \sim 6.9$ keV has already been found by Ballantyne et al. (2004), who analysed an XMM observation of this source. The new fit results in the second line to be at $E = 6.96^{+0.08}_{-0.10}$ keV.

Moreover, the addition of a second line for *SWIFT J1838.4-6524* led to a better fit with $\Delta\chi^2 = 7$. The new line was centered at $E = 6.86 \pm 0.06$ keV. The same was true for two more sources. The fit was improved significantly, $\Delta\chi^2 = 10$ and 53, for the sources *SWIFT J1347.4-6033* and *J1836.9-5924*, respectively, when a second gaussian emission line was added to the model. The best-fit energy of the new line in the former source was $E = 6.88 \pm 0.06$ keV and $E = 7.13 \pm 0.05$ keV for the latter one. For the five aforementioned sources the additional line may be explained as fluorescence from highly ionised, probably H-like, Fe atoms.

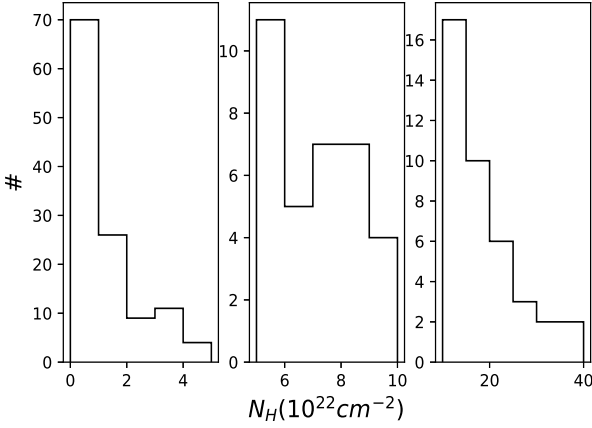
In addition to the sources with more than one emission lines, there were sources for which the fit resulted in a broad Fe $K\alpha$ line and no supplementary line was evident in the residuals. We fitted the corresponding spectra with the line width free to be minimised. There were nine such sources in total. Their names and the best-fit values of the line width are listed in Table 1.

3.3. Classification

Before proceeding to the analysis of the spectral results, we found it useful to divide the sources into three groups based on their best-fit N_H value. In this way, we were able to study the evolution of spectra as the absorption increases and to look for similarities and differences between the different groups. We chose to follow an N_H -based classification, because N_H has a direct physical interpretation; it only depends on the amount of gas lying in our line of sight, and because differences in N_H can be simply

Table 1: Sources with a broad emission line.

Source Name	$\sigma_{Fe}(keV)$
SWIFT J0123.9-5846	0.21 ± 0.03
SWIFT J0244.8+6227	0.60 ± 0.09
SWIFT J0521.0-2522	$0.75^{+0.13}_{-0.10}$
SWIFT J0925.0+5218	$0.30^{+0.05}_{-0.04}$
SWIFT J1145.6-1819	0.40 ± 0.08
SWIFT J1315.8+4420	$0.33^{+0.06}_{-0.05}$
SWIFT J1349.3-3018	0.19 ± 0.03
SWIFT J1741.9-1211	$0.40^{+0.12}_{-0.10}$
SWIFT J1835.0+3240	0.30 ± 0.08

Fig. 2: Distribution of the best-fit N_H in the different classes, UNOB (left), LOB (central), and MOB (right panel).Table 2: Number of sources in the N_H -based defined classes.

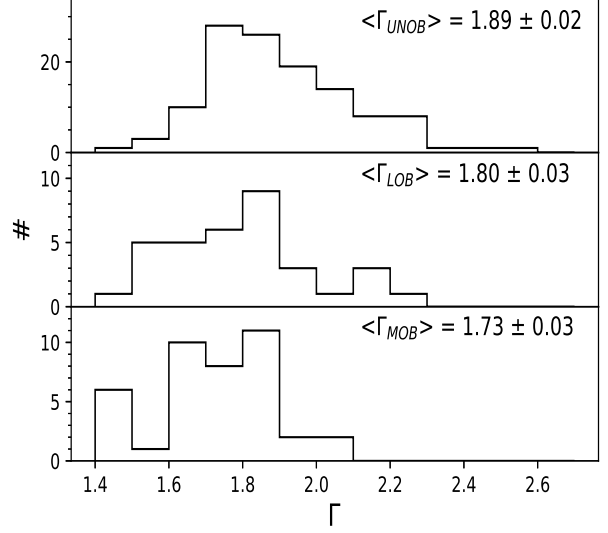
	Class 4	Class 5	Total
UNOB	92	28	120
LOB	10	24	34
MOB	5	48	53

interpreted as differences in the source’s inclination according to the unification model. In total, we defined three groups, the unobscured ($N_H < 5 \cdot 10^{22} \text{ cm}^{-2}$, UNOB), the lightly obscured ($5 \cdot 10^{22} \text{ cm}^{-2} < N_H < 10^{23} \text{ cm}^{-2}$, LOB), and the mildly obscured ($N_H > 10^{23} \text{ cm}^{-2}$, MOB) class. We chose an N_H value of $5 \cdot 10^{22} \text{ cm}^{-2}$ as the boundary between UNOB and LOB sources because N_H values much smaller than this cannot be well constrained by fitting NuSTAR spectra, which start at 3 keV. The number of sources in each group versus their optical classification is given in Table 2. Figure 2 plots the distribution of N_H in each class.

4. Results

4.1. The photon index

It is generally accepted that the X-ray AGN emission above 2 keV is mainly produced by Comptonisation of ultraviolet and optical photons in an optically thin region. Such an emission is well described by a power law. The power-law slope mainly depends on the accretion rate and on the corona’s physical properties. As a result, variations in Γ can be used to probe variations

Fig. 3: Distribution of the best-fit Γ in the UNOB (top), LOB (middle), and MOB (bottom panel) class.

close to the black hole. AGN spectra have been found to exhibit a large range of indices, from around 1.5 up to almost 2.5 with a mean value of around 1.8 (e.g. Ricci et al. 2017).

Figure 3 plots the distribution of Γ , which seems to vary in each class. The main difference is that MOB sources occupy a shorter range of values than the other two classes, while sources with $\Gamma > 2.1$ are found only in less obscured, UNOB and LOB, groups. In addition, the photon index decreases with N_H , with the average value in each class being 1.89 ± 0.02 , 1.80 ± 0.03 , and 1.73 ± 0.03 , respectively.

We evaluated the statistical significance of the difference in Γ distributions using the Kolmogorov-Smirnov test. The LOB distribution was found to not be significantly different to neither the MOB nor the UNOB distribution. On the other hand, the difference between the distribution of UNOB and MOB sources was found to be significant, with a null hypothesis probability of $P_{null} = 0.1\%$. The difference in the mean values between the two classes is $D\Gamma = 0.16 \pm 0.04$, and, hence, the two values are different even at a $3\text{-}\sigma$ level. As discussed in Sect. 5.1, the observed difference might be explained if a specific geometry is assumed for the X-ray source or if the corona is intrinsically different between highly absorbed and unabsorbed sources.

4.2. The high-energy cutoff

The high-energy cutoff may be viewed as a proxy for the temperature of the X-ray source. As a result, its knowledge provides information about the corona’s dynamics and the physical processes that take place inside it (e.g. Fabian et al. 2015). Although a detailed discussion of the cutoff energy in individual sources is outside the scope of this work, some simple remarks could still be made.

The penultimate column of Table 6 lists the best-fit values of the cutoff energy. For most of the sources it was not constrained and only a lower limit was derived. This was expected since the cutoff energy cannot be constrained when its real value is much higher than the energies probed by NuSTAR, or when the observation exposure and the source brightness are not high enough

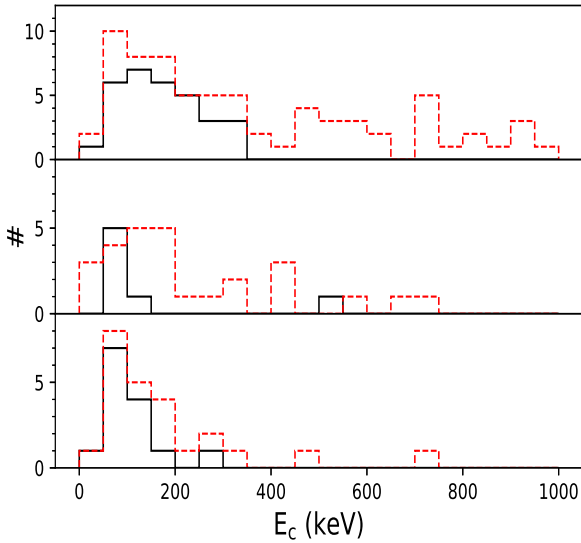


Fig. 4: Distribution of the best-fit E_c in the UNOB (top), LOB (middle), and MOB (bottom panel) class. The solid black lines denote the distributions of the well constrained values and the red dashed lines denote the distribution of the estimated lower limits.

to allow its detection. More precisely, we constrained the cutoff for 55 sources and a lower limit was estimated for 152 sources. Taking into account only the well constrained values, the average high-energy cutoff for the total sample was found to be $E_c = 149 \pm 14$ keV. This value is consistent with the results of Molina et al. (2019) and Malizia et al. (2014), who studied the hard X-ray spectrum of a sample of Type 1 AGN using NuSTAR and INTEGRAL, respectively. In the contrary, the calculated average is smaller than the value estimated by Ricci et al. (2017) when they studied the BAT spectrum of Swift/BAT AGN taking into account the whole sample and it is also smaller than the value found by Ballantyne (2014) by fitting the luminosity function of local AGN. This apparent discrepancy is probably due to the fact that we only consider the constrained cutoffs in deriving the average value.

The distribution of cutoff in the three different classes is plotted in Fig. 4. Using the Kolmogorov-Smirnov test and considering only the constrained values we found that no statistically significant difference was present between the different categories ($P_{null} > 1\%$). Furthermore, by estimating the corresponding Spearman's rank correlation, we looked for potential correlations between the high-energy cutoff and the other parameters. No statistically significant (P_{null} was higher than 1% in all cases) correlation was found between E_c and Γ , R , and the X-ray luminosity of the source (Sect. 4.4).

4.3. The reflection strength

The reflection parameter, R , provides an estimation of how strong the reflected emission is with respect to the continuum power law. For a given inclination angle, $R = 1$ corresponds to an isotropic X-ray source illuminating a slab disc. Constraining R is important since its value provides information on the geometry of the source. In addition, the value of R affects significantly the fraction of Compton thick sources estimated by

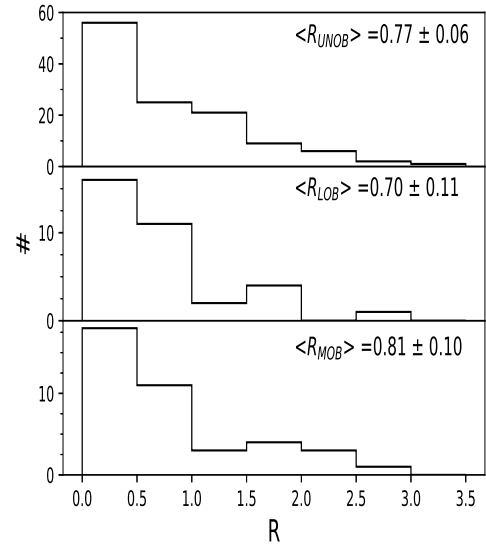


Fig. 5: Distribution of the best-fit R in the UNOB (top), LOB (middle), and MOB (bottom panel) class.

cosmic X-ray background (CXB hereafter) population synthesis models. Since the two parameters are degenerated in reproducing the CXB spectrum, increasing R decreases significantly the fraction of Compton thick AGN in the Universe.

Although several works have been conducted on determining R in the various classes of AGN, its value is still debated. The results in the literature can often be contradictory and span a large range of values. Moreover, R has been found to be correlated to other spectral or physical parameters of AGN. For instance, Zdziarski et al. (1999) found a positive correlation between R and the spectral index, Γ . More recent studies have suggested a dependence of R on the observed N_H (Ricci et al. 2011) and X-ray luminosity (Del Moro et al. 2017). However, most of the results have been based on the analysis of average spectra. NuSTAR, being the first hard X-ray focusing telescope, provides a unique opportunity to study the evolution of reflection strength in individual sources to unprecedented detail.

Figure 5 plots the distribution of R in the different classes. The three distributions look similar and no significant statistical difference was found. The average best-fit value for the total sample is $\langle R \rangle = 0.78 \pm 0.05$. This is smaller than the usually assumed value of $R = 1$ in CXB synthesis models, which is also expected for a simple disc reflection. However, our value is consistent within the errors with the estimations of previous studies (e.g. Ricci et al. 2011; Vasudevan et al. 2013).

The mean value of reflection is $\langle R \rangle = 0.77 \pm 0.06$, 0.70 ± 0.11 , and 0.81 ± 0.10 for the UNOB, LOB, and MOB sources, respectively. The mean values are fully consistent within the errors. This consistency is not easily explained within the simple unification model. To a first approximation, the reflection emission results from the scattering of the continuum power-law by the disc and torus surfaces. According to the unification model, the more obscured sources are observed at higher inclinations and, thus, the disc reflection is expected to be suppressed in the LOB and especially MOB sources due to geometric effects. If the torus is assumed to be similar in all AGN, then a decrease of R with N_H should be expected. The disagreement between

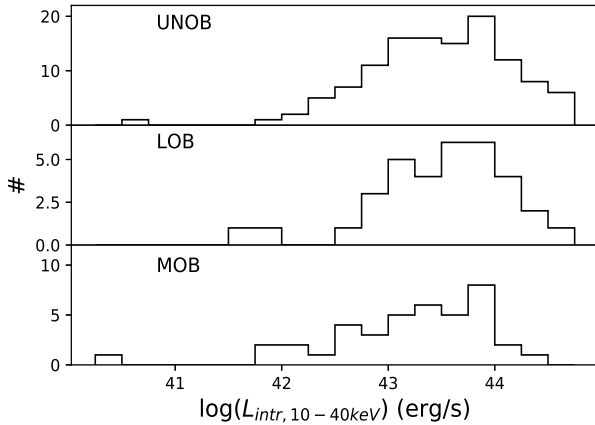


Fig. 6: Intrinsic 10-40 keV luminosity distribution in UNOB (top), LOB (middle), and MOB (bottom panel) sources.

this expectation and our results suggests that a more complicated mechanism is at work.

Strong reflection in highly absorbed sources has been firstly observed by Ricci et al. (2011) using INTEGRAL observations and was later verified by Vasudevan et al. (2013) and Esposito & Walter (2016) using BAT data. This result could be explained if the covering factor of torus as observed by the central X-ray source is increasing with absorption. Hence, the total reflection would remain roughly constant despite the decrease of disc reflection. In a case of a clumpy torus, such an increase would correspond to an increase in the opening angle of the torus or to an increase of the clouds' filling factor.

4.4. 10-40 keV Luminosity

Using the best-fit results we estimated the X-ray luminosity of each source from 10 to 40 keV. We calculated the intrinsic, meaning unabsorbed, luminosity and the corona luminosity, that is the luminosity predicted solely by the power-law emission component. The luminosity of MOB sources, which are the only sources with $N_H > 10^{23} \text{cm}^{-2}$, was also corrected for Thomson scattering because this is not taken into account by the used *zphabs* model. The Thomson correction for sources with $N_H < 10^{23} \text{cm}^{-2}$ is smaller than 7% having an insignificant effect to the results and was, thus, safely omitted for UNOB and LOB sources.

Figures 6 and 7 plot the distributions of intrinsic and corona luminosity, respectively. A visual examination of these figures reveals the similarity of the distributions in the different classes. The luminosities occupy a similar range of values in every class, with the majority of sources found in the range $42.5 < \log(L_{\text{intr}, 10-40\text{keV}}) < 44$ in units of erg/s. There are only two sources, one in MOB and one in UNOB class, with an intrinsic luminosity $\log(L_{\text{intr}, 10-40\text{keV}}) < 41.5$ erg/s. While there is a tentative feature that highly luminous sources with $\log(L_{\text{intr}, 10-40\text{keV}}) > 44$ erg/s are found mainly in a less obscured state, this result is not statistically significant. Moreover, the lack of any significant difference between the three classes was further supported by the results of the Kolmogorov-Smirnov test. However, this observed similarity is not surprising. The intrinsic source luminosity is expected to exhibit similar values regardless of the absorption state as the same central engine is assumed.

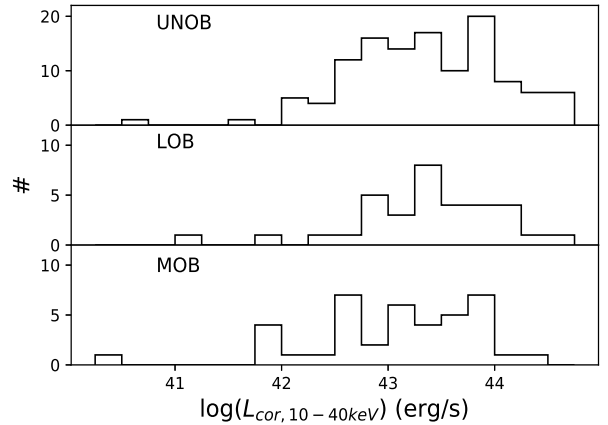


Fig. 7: Distribution of corona luminosity in the 10-40 keV energy range for UNOB (top), LOB (middle), and MOB (bottom panel) sources.

There have been numerous studies investigating the correlation of spectral parameters with X-ray luminosity. The existence of such correlations might shed light on the physical processes producing the different emission components. We, therefore, examined our results for the existence of any such correlation, as well.

The reflection strength was found to be slightly anti-correlated to the X-ray luminosity for the UNOB sources. A stronger correlation was found with the corona luminosity than with the intrinsic luminosity. The latter includes contribution from the reflected emission and is, consequently, expected to exhibit a weaker correlation. We calculated the Spearman's rank correlation coefficient between R and $L_{\text{cor}, 10-40\text{keV}}$ to be $\rho = -0.36$ with a chance probability of $P_{\text{null}} = 5 \cdot 10^{-5}$. However, it is likely that this correlation is observed only due to the selected sample. Sources with low power-law 10-40 keV luminosity are less likely to be detected by BAT, which is sensitive to photons with energy above 15 keV. It is then reasonable to assume that these sources would only be observed if they feature a strong reflection emission, which would render them brighter in total. A more detailed analysis taking into account the selection effects is needed before a robust conclusion on the reality of $R - L_{\text{cor}, 10-40\text{keV}}$ correlation can be made.

The reflection strength was not found to be correlated with the X-ray luminosity for either the LOB or the MOB sources. Moreover, no statistically significant ($P_{\text{null}} < 1\%$) correlation was found between the power-law index and the X-ray luminosity in either of the considered classes, consistent with previous studies (e.g. Winter et al. 2009).

4.5. $R - \Gamma$ correlation

In Panagiotou & Walter (2019), we found that the reflection strength is positively correlated with the power-law index for unobscured sources. In the following, we examine the validity of this correlation in a much bigger sample and we discuss possible physical scenarios that could produce such a correlation.

4.5.1. Unobscured sources

The dependence of R on Γ for the UNOB class is plotted in Fig. 8. The two parameters are clearly correlated. However, they are

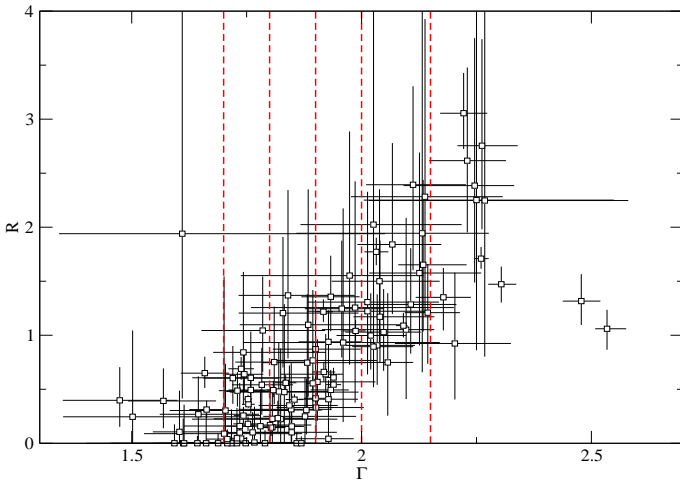


Fig. 8: R - Γ correlation in UNOB sources. The vertical dashed lines indicate the boundaries between the different subgroups as defined in Sect. 4.5.1.

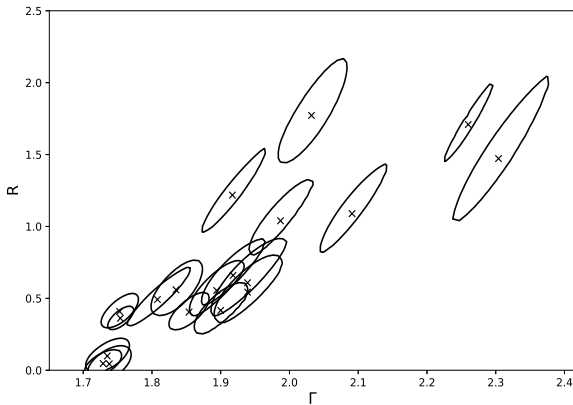


Fig. 9: Observed R - Γ correlation for the UNOB sources with well constrained Γ (see text for details). The error contours correspond to a 99% confidence interval ($\Delta\chi^2 = 9.21$).

also degenerated, meaning that they are intrinsically correlated in the model. Consequently, a robust conclusion cannot be made by a simple visual examination of the scatter plot. We followed different approaches in order to verify that the observed correlation is real.

Firstly, we restricted our sample to the sources with high quality data. More precisely, we studied only the sources for which Γ is well constrained, with a $1-\sigma$ relative error of $\frac{\Delta\Gamma}{\Gamma} < 0.0135$. There were 19 such sources. For each one of them, we calculated their error contour using the *steppar* command in XSPEC. The results are plotted in Fig. 9. The plotted contours correspond to a confidence interval of 99% ($\Delta\chi^2 = 9.21$). The general trend of R increasing on average with Γ is well observed. It is evident that the best-fit values are not consistent within the errors, and their differences cannot be explained by the observed degeneracy.

Furthermore, we produced simulated spectra to assess how the model's degeneracy affects the estimation of the two param-

eters. Using the NuSTAR responses, we simulated³ the spectra expected to be observed from sources with emission given by the *pexrav* model. Spectra were produced for the same value of reflection strength, equal to the average value of UNOB objects, $R = \langle R_{UNOB} \rangle = 0.77$ and for six different values of spectral indices, $\Gamma = 1.6, 1.75, 1.85, 1.95, 2.07$, and 2.25 . These values correspond roughly to the mean values of each subgroup defined below in Sect. 4.5.1. For each Γ , 200 simulated spectra were produced assuming a power-law normalisation equal to the mean value of each subgroup and an exposure time of 25 ks. We then fitted the simulated data with the *pexrav* model and calculated the mean R and Γ for each group of simulated spectra in order to evaluate whether the observed trend could be an artifact of the quality of our data and the model's degeneracy. The estimated mean values are plotted as green diamonds in Fig. 10. It is evident that the model's degeneracy does not reproduce an average increase of reflection with the power-law slope. The R values are consistent to the mean value within the errors. We, therefore, concluded that the observed correlation is real. The reality of this correlation for a smaller sample of sources and at lower energies was also studied in detail and confirmed by Zdziarski et al. (2003).

Having confirmed the reality of the observed correlation, it should be noted that this is not a 1:1 correlation. There are two main reasons why scattering around a single line correlation is expected. Firstly, statistical errors might result in a scatter around the real correlation. Secondly, and more importantly, a prominent scatter around a 1:1 correlation is expected because of the physical differences in different AGN. AGN are really dynamic systems occupying a range of black hole mass, accretion rate, black holes spin, and several other physical parameters that would define the system uniquely. It is then expected that, for example, two sources with the same reflection strength could have different power-law slopes as a result of the intrinsic physical differences between them. Therefore, the observed trend suggests that only on average sources with higher reflection strength would also feature steeper spectra for the continuum emission.

In order to improve the statistics, we did not consider the best-fit values of the individual sources in the following analysis. Instead, we divided the UNOB sources into six groups based on their best-fit Γ value and estimated the mean value of the individual fits for both R and Γ in each group. The boundaries of each group are denoted by vertical red dashed lines in Fig. 8. In addition, we calculated the stacked spectrum of each subgroup. In deriving the stacked spectra we renormalised each individual spectrum before adding with respect to its ARF file in order to account for differences in the source's size. The stacked spectra were calculated using the *mathpha* tool and were then binned so that each bin contains at least 100 source counts.

Figure 10 plots the dependence of R on Γ after grouping the sources. The black open squares denote the mean values of the individual fits, taking into account all the UNOB sources, and the red filled circles denote the best-fit values of the stacked spectra. The two sets predict a similar correlation trend, providing extra evidence that this is a real correlation. The explanation of this trend by physically motivated models is discussed in Sect. 5.2.

4.5.2. The special case of SWIFT J0947.6-3057

SWIFT J0947.6-3057 was observed five times with NuSTAR from July 2012 until March 2015. We fitted all the five spectra of

³ The simulated spectra were produced using the *fakeit* command in XSPEC.

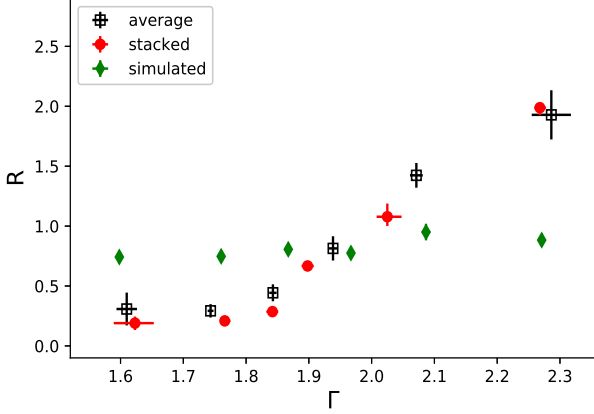


Fig. 10: Observed R - Γ correlation for the subgroups of UNOB class. The red filled circles correspond to the best-fit values of the stacked spectra, while the black open squares to the average values of the individual best fits. The green diamonds correspond to the mean values retrieved for the simulated data. The errors are not distinguishable because of their small value.

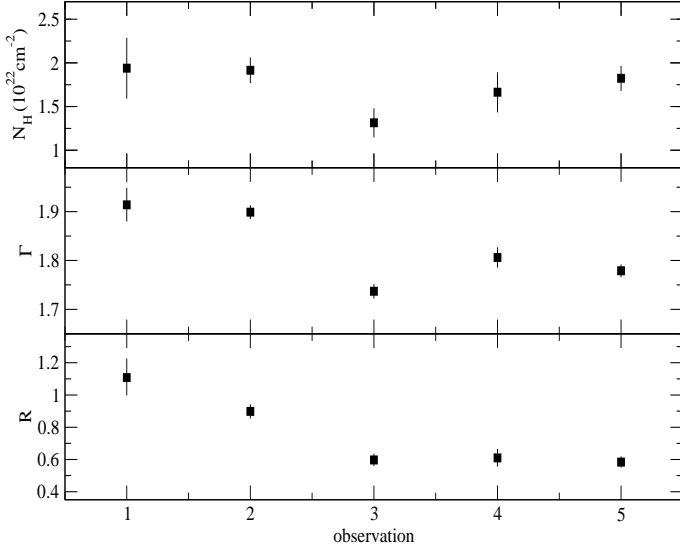


Fig. 11: Best-fit absorption column density (top), spectral index (middle), and reflection strength (bottom panel) for SWIFT J0947.6-3057. The x axis corresponds to an increasing number of observation.

the source with the baseline model (Sect. 3.1). The best-fit results are listed in Table 6 and plotted in Fig. 11. *SWIFT* J0947.6-3057 is the only object of our sample that exhibits a strong variation in the power-law slope and reflection strength, while its absorption level remains roughly constant. The lack of variability for N_H is supported by a χ^2 test ($P_{null} = 10\%$), unlike for Γ and R . This feature let us study the variations of R with respect to Γ variations for an individual source.

Figure 12 plots the best-fit R as a function of Γ . The crosses indicate the best-fit values and the ellipses denote the best-fit contour of the two parameters at a 99% confidence interval, as calculated using the *steppar* command in XSPEC. The observed correlation cannot be explained due to the statistical errors or

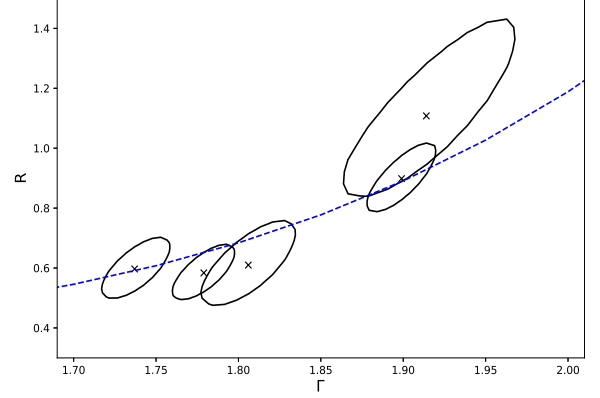


Fig. 12: R - Γ correlation in SWIFT J0947.6-3057. The x symbols indicate the best-fit values, while the error contours correspond to a 99% confidence level ($\Delta\chi^2 = 9.21$). The dashed blue line indicates the correlation expected for a moving corona (Sect. 5.2). It is similar to the one plotted in Fig. 16, but a constant of $R = 0.25$ has been added to it.

the degeneracy of the two parameters. We concluded that this is a real correlation, intrinsic in the emission of the source.

Zoghbi et al. (2017) have suggested that an apparent correlation between the reflection strength and the photon index might be observed for a single source even when the reflected emission remains constant. The emission from a distant reflector smooths out the variability of the primary continuum and, consequently, two observations might exhibit the same amount of reflected emission but a different continuum power law. If the continuum is steeper in one observation, then the reflection strength in this observation will also be larger in order to match the observed reflected flux. Therefore, the observed correlation might be an artifact of the model fitting. However, this is not the case for *SWIFT* J0947.6-3057. Using our best-fit results, we confirmed that the observations of larger R feature higher flux of reflected emission, as well. In other words, the increase in Γ was found to correspond to an increase in the flux of the reflected emission, excluding the possibility that the observed correlation is an artifact of the fit. This is further supported by the results of Zoghbi et al. (2014). These authors found that the Compton hump emission lags behind the continuum power-law by ~ 1 ks, strongly favouring a disc reflection for large part of this emission, instead of a distant reflector; while, the existence of an R - Γ correlation requires the disc to be the main reflector, as well (Sect. 5.2).

An R - Γ correlation has been observed before for a group of Seyfert galaxies (e.g. Zdziarski et al. 1999). However, to the best of our knowledge, this is the first time that a positive correlation is found for an individual AGN with such a high statistical significance. The importance of this result lies, among other things, on the fact that this would provide further constraints on the proposed explanations of the R - Γ dependence, if the same driving mechanism is assumed. This mechanism should be able to account for both variations in the local environment of an AGN and variations between different sources.

As discussed in Sect. 5.2, the most promising model to explain the observed correlation is that of an X-ray source moving with respect to the disc. The dashed blue line in Fig. 12 plots the predicted relation of this model. No fitting of this line has been applied to the data, but a constant value of $R = 0.25$ has been

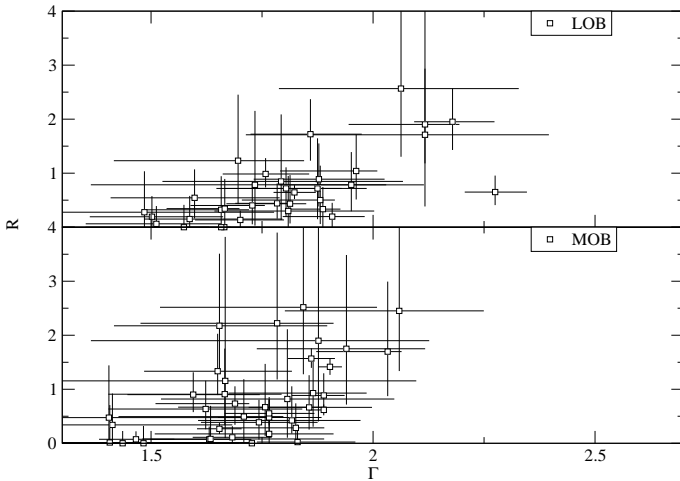


Fig. 13: Best-fit reflection strength against power-law slope for the LOB (upper) and MOB (lower panel) sources. The axes are of the same scale as in Fig. 8.

added to the predicted values in order for them to match the observed ones. This amount of reflection might be attributed to the reflection originating from a second scattering surface, like the surrounding torus. *SWIFT J0947.6-3057* is a Seyfert 2 galaxy and a torus contribution to the reflection emission is not surprising. The predicted line is fully consistent with the observed values within the errors.

4.5.3. Obscured sources

We have shown previously that an R - Γ correlation is not observed for the obscured sources, pointing to a different behaviour of the reflection emission between obscured and unobscured AGN (Panagiotou & Walter 2019). The lack of an R - Γ correlation is, however, not unexpected in this case. In general, the obscured sources are assumed to be observed at higher inclination angles and, thus, less disc emission will be observed. Therefore, a subtler correlation is expected to be observed, if any.

Figure 13 plots the best-fit R versus Γ for the obscured sources, that is for both LOB and MOB objects. The axes are of the same scale as in Fig. 8 to allow for a direct comparison. The two parameters seem to be only slightly correlated, but a visual examination of Fig. 13 does not allow for a robust conclusion on the existence of a positive correlation. Interestingly enough though, the sources in LOB class exhibit slightly stronger evidence of a correlation.

To evaluate the existence of a real correlation, the degeneracy of the two model parameters has again to be taken into account. Due to the larger errors and the smaller amount of objects in the MOB and LOB classes, there are not sufficiently enough sources with well constrained Γ to allow studying a subsample of high quality data, similarly to the analysis followed in Sect. 4.5.1. Instead, we produced simulated data to examine the reality of the observed trend.

We generated two groups of simulated spectra. Initially, 200 spectra were generated assuming a *pexrav* model for the source emission with a reflection, spectral index and power-law normalisation equal to the average values of the best-fit results for LOB sources. An exposure time of 25 ks was assumed and the NuSTAR responses were utilised. The simulated spectra were then fitted using the *pexrav* model and the resulted R - Γ values were fitted by a straight line. In this way, we were able to measure and

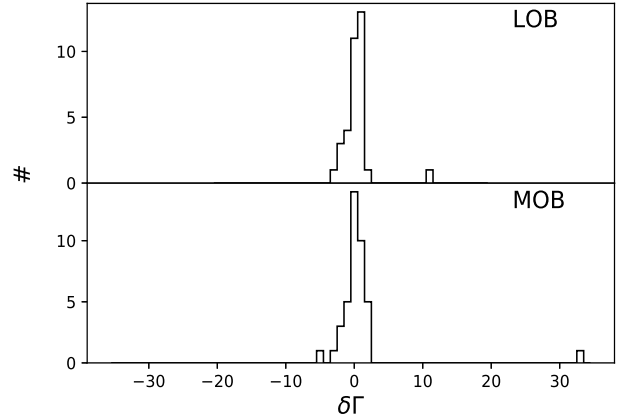


Fig. 14: Histogram of the quantity $\delta\Gamma$, as defined in Sect. 4.5.3 for the two classes of obscured objects.

describe in an analytical form the apparent correlation produced by the model's degeneracy. The same procedure was followed to produce another 200 fake spectra, using this time the best fit results of the MOB sources. Eventually, we had parametrised the degeneracy expected for the two classes by two straight lines.

In the following, we tested if the R - Γ trend observed in the obscured sources could be produced by the model's degeneracy. To that extent, we assumed that all the sources of each class have the same R value, equal to the corresponding average value, and the observed difference between this value and the measured one is the result of the degeneracy. Having parametrised this degeneracy by a straight line, we were able to project every measured point (R, Γ) onto the line $R = \langle R \rangle$ and as a result, estimate a new value for the power-law slope, Γ_d . This new value corresponds to the real value of the power-law emission under the assumption of a constant R . If this new value deviates significantly from the initially calculated best-fit Γ , then the hypothesis of constant R is probably wrong. If, instead, the two values are consistent within the errors, the hypothesis cannot be rejected.

Figure 14 plots the histogram of this deviation quantified as $\delta\Gamma = \frac{\Gamma - \Gamma_d}{\Delta\Gamma}$, where $\Delta\Gamma$ is the error of the best-fit value Γ . The upper and lower panel correspond to the LOB and MOB sources, respectively. Figure 15 is a zoomed version of Fig. 14. It should be noted that the histogram in Fig. 15 has been renormalised, meaning that the source density, instead of the number of sources, is plotted in this figure. The blue solid line denotes the normal distribution of zero mean and unity standard deviation. No fit has been applied to the histogram.

Only one LOB and one MOB source exhibit a strong deviation between the best-fit Γ and the one predicted under the assumption of constant reflection. The deviation in the remaining sources seem to be consistent with zero within the errors. This implies that only for a few sources a different value of reflection is statistically required. Taking into account the simplicity of our initial hypothesis and the diversity of AGN, our main conclusion is that the quality of the data does not allow for a statistically robust detection of an R - Γ correlation in the obscured sources. The observed trend can be well explained as the result of the model's degeneracy. Instead, there seems to be a correlation between R and N_H in these sources. A detailed study of this correlation will be presented in an upcoming paper.

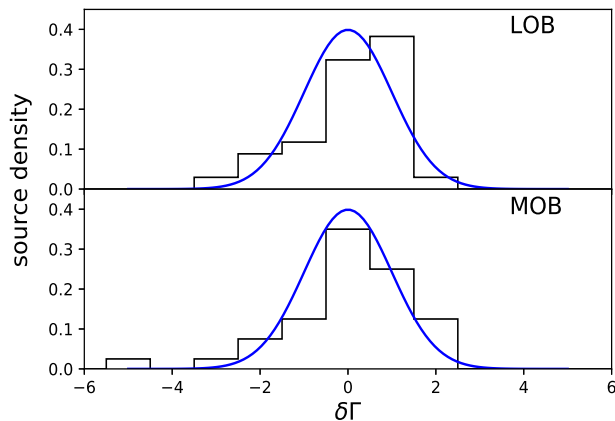


Fig. 15: $\delta\Gamma$ normalised histogram. One LOB (upper panel) and one MOB (lower panel) source lie outside the plotting range. The blue solid line is the same in both panels and corresponds to the standard normal distribution.

5. Discussion

5.1. Γ discrepancy

The applied analysis revealed a difference in the power-law slopes between unabsorbed and heavily absorbed sources. While there was no prominent disagreement between the Γ distributions of LOB and the other two classes, MOB sources were found to exhibit harder spectra than UNOB sources. A Kolmogorov-Smirnov test confirmed the statistical significance of this difference ($P_{\text{mult}} = 0.1\%$), with the mean Γ values of the two classes differing by $D\Gamma = 0.16 \pm 0.04$.

We checked whether the observed difference could be a selection effect of the used sample. More precisely, we examined if the MOB sources are intrinsically less luminous than the UNOB or if the UNOB objects with large best-fit Γ are less luminous in comparison to UNOB sources with small Γ . Any of these two cases, might lead to high- Γ MOB sources not being detected by BAT due to their high absorption. In Sect. 4.4, we estimated the corona luminosity of all the sources in the energy range 10-40 keV. This energy range is well probed by NuSTAR for most of our sources and highly overlaps with the energy range of BAT. We found no significant differences between the luminosity of MOB and UNOB sources or between the luminosity of sources with different Γ . As a result, we concluded that the difference in the Γ distributions is real and not a selection effect.

Since the AGN X-ray continuum is the result of Comptonisation, a harder spectrum, meaning smaller Γ , is expected from an optically thicker Comptonising region. Assuming that UNOB and MOB AGN feature no intrinsic differences in the physical properties of the X-ray source, a higher optical depth in MOB sources indicates that soft photons spend on average more time within the X-ray source in absorbed sources than in unabsorbed ones. This might be achieved if a slab geometry is assumed for the corona. According to the unification model, highly absorbed sources are observed on average at higher inclination angles than unabsorbed sources. If the corona is homogeneous and of a slab shape, then the photons emitted closer to edge-on had on average longer paths to travel within the corona, and thus correspond to larger optical depth.

Using the *compps* model (Poutanen & Svensson 1996) in XSPEC, we confirmed that a slab corona would produce a harder

spectrum when observed closer to edge-on. The difference between the edge-on and face-on Γ was estimated to be about 0.07 for vertical optical depths of $\tau \sim 1$. This value is somewhat smaller than the observed discrepancy ($D\Gamma = 0.16 \pm 0.04$), but consistent to it within $\sim 2.3 \sigma$. If such a high difference in Γ is indeed verified with higher significance, inclination effects might only be partly contributing to this discrepancy.

The observed disagreement might also be explained if different parts of the X-ray source are observed in the different classes. For example, it is reasonable to assume that the X-ray source is vertically extended above the disc. Sources observed close to face-on will then be dominated by the emission of the source's top part, while sources of higher inclination will feature emission from both upper and lower regions of the X-ray source. If a specific vertical structure of the X-ray source is assumed, which could, for instance, be variations in its temperature profile, one may expect a different spectral shape for the emission originating from different layers of the source. Although tempting, a detailed estimation of the expected discrepancy in this case would require the knowledge of the X-ray position source and its structure. Such an analysis is outside the scope of this work.

5.2. Physical interpretation of the R - Γ correlation

The results of the spectral analysis suggested a positive correlation between the reflection strength and the spectral index for the UNOB sources. The R - Γ correlation may provide information about the inner geometry of AGN. The power-law index describes the shape of a Comptonisation spectrum and it, thus, depends on the flux and spectrum of seed disc photons and on the physical state of the corona. On the other hand, the reflection strength depends on the X-ray primary continuum emission and on the characteristics of the scattering surface that produces the reflection emission. It is then evident that the two parameters can be correlated only if the disc is the primary reflector in the UNOB sources. This result is further supported by the detection of high-frequency soft or Fe $K\alpha$ lags in the emission of several UNOB sources. These lags, usually of the order of ten to hundreds of seconds, correspond to time difference between variations in the X-ray continuum and variations in the soft X-rays or Fe line, with the continuum driving the variability. It has been argued that the observed lags can be explained if the delayed emission is produced due to scattering of the inner disc surface (e.g. Fabian et al. 2009). In total, at least seven sources have been found to exhibit a soft lag and seven sources exhibit a Fe lag (De Marco et al. 2013; Kara et al. 2016, and references therein).

It should also be noted that R exhibits values importantly higher than 1 for $\Gamma > 2.0$. If a thin disc is the sole reflector of the primary emission, such high values of reflection strength are not easily explained and an anisotropy of the X-ray source or some relativistic effects have to be assumed.

Moreover, the exact shape of the correlation provides important constraints on the geometry or the physical interplay between the disc and the corona. Zdziarski et al. (1999) were the first to observe a positive correlation between the reflection strength and the power-law index in Seyfert galaxies. They concluded that such a correlation could be explained if the corona is moving with respect to the disc, a model derived by Beloborodov (1999). In this model, magnetic flares are produced above the disc with a slightly relativistic velocity. When the flare is moving away from the disc, relativistic aberration reduces the amount of photons emitted towards the disc and subsequently the reflected emis-

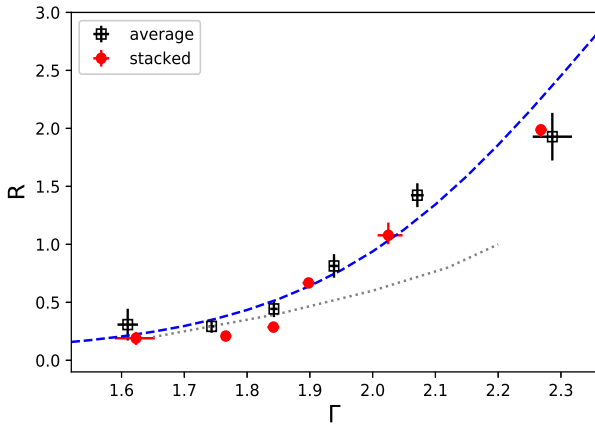


Fig. 16: Observed R - Γ correlation for the subgroups of UNOB class. The red filled circles correspond to the best-fit values of the stacked spectra, while the black open squares to the average values of the individual best fits. The errors are not distinguishable because of their small value. The dashed blue line indicates the correlation expected for a moving corona with respect to the disc (Beloborodov 1999) and the dotted gray line indicates the correlation predicted for a variable covering disc factor.

sion, which also leads to a harder spectrum. The opposite trend is expected when the flare is moving towards the disc.

Figure 16 plots the observed $R - \Gamma$ correlation, exactly as in Fig. 10. Using the equations of Beloborodov (1999), we calculated the correlation predicted for a moving X-ray source, which is plotted as a blue dashed line in Fig. 16. The blue line was produced assuming a disc albedo of $\alpha = 0.15$, a system inclination of $\cos i = 0.45$, and a value of 0.55 for the geometry-dependent parameter μ_s , which is defined in the aforementioned paper. No fitting was performed of this line to the data. The predicted correlation seems to explain the observed trend well.

The model requires a velocity range of $-0.3 < \beta < 0.6$ for the observed range of Γ and R to be reproduced, where β is the source velocity in units of light speed and the minus sign indicates move towards the disc. The deduced velocities are only mildly relativistic. Although it is difficult to conceive a mechanism to accelerate the X-ray source both outwards and towards the disc, this possibility cannot be excluded. For example, Beloborodov (1999) proposed a radiatively driven acceleration mechanism.

This model is able to explain the observed correlation for *SWIFT J0947.6-3057*, as well. The variation in Γ for this object suggests a variation in the source velocity from ~ 0.4 to ~ 0.16 in units of light speed, which is not unreasonably high. Since variations in the source velocity are expected to depend on variations of the inner disc, where the source is formed, the observed velocity variability could be achieved within the spectral variability timescale of *SWIFT J0947.6-3057*.

The predicted correlation for this object is plotted in Fig. 12 as a blue dashed line. A constant value of $R = 0.25$ has been added to this line in comparison to the line of Fig. 16 in order to match the observed values. This extra emission might be the result of additional reflection from surrounding material. The predicted correlation reproduces well the observed trend within the errors.

A positive R - Γ correlation might also be produced if the disc covering factor as observed from the primary X-ray source is

variable. It has been suggested that the continuum X-ray emission might originate from a hot optically thin flow in the inner part of the disc. In this configuration, matter accretes in the form of a Shakura-Sunyaev disc (Shakura & Sunyaev 1973) until a specific radius, after which the disc is truncated. At radii smaller than the truncation radius, a complicated accretion might be in place, with hot optically thin accretion flow and cold clumps of an optically thick accretion disc coexisting. Recently, Poutanen et al. (2018) studied the spectral emission for such a configuration. They found that for a given ionisation level the power-law index and the disc covering factor, f_c , are positively correlated (Fig. 5 in their paper). Since for a given inclination angle the reflection strength corresponds to the reflector's covering factor, the above result predicts a correlation between Γ and R , as well. Using their results and for $R = f_c$, we calculated the predicted correlation, which is plotted as a gray dotted line in Fig. 16. The model predicts a weaker correlation than the observed one and is unable to probe all the observed values. The power-law slope could reach values above 2.2 if disc dissipation is assumed. However, the reflection strength might reach values above unity only if some relativistic beaming is assumed or under the assumption of an anisotropic source.

The existence of the correlation for a single source renders this model even less plausible. Variations of the disc covering factor in one source are expected to happen at timescales similar to or larger than the viscous timescale, which is given in seconds by (Frank et al. 2002):

$$t_{\text{visc}} \sim 3 \times 10^5 \alpha^{-4/5} \dot{M}_{16}^{-3/10} M_1^{1/4} R_{10}^{5/4}, \quad (2)$$

where α is the parameter describing the disc viscosity, \dot{M}_{16} is the mass accretion rate in units of 10^{16} g/s , M_1 is the black hole mass in units of solar masses and $R_{10} = R/(10^{10} \text{ cm})$. For an accretion rate $\dot{M} = 0.05 \dot{m}_{\text{Edd}}$ (\dot{m}_{Edd} is the Eddington accretion rate), a black hole mass of $M_{\text{BH}} = 2 \cdot 10^6$ solar masses (Wang & Zhang 2007), and assuming a viscosity parameter of $\alpha = 0.1$, the viscous timescale at $R = 50 R_g$ (R_g is the gravitational radius) for *SWIFT J0947.6-3057* is of the order of 150 years. However, R and Γ seem to vary significantly within 2 years. As a result, this variation cannot be explained by variations in the disc geometry.

Another possible way for the reflection strength to vary would be if the position of the corona with respect to the black hole is changing. Assuming a lamp post geometry, the reflection strength will increase when the corona is located closer to the black hole because gravitational effects would lead to the illumination of disc by a larger flux than the one observed along our line of sight. However, it is not a straightforward exercise to imagine why the power-law slope would then also increase. One possible solution would be if the seed disc emission observed by the corona is higher, leading to faster cooling and consequently to a softer spectrum. At first approximation, however, and ignoring relativistic effects, the disc emission intercepted by a region closer to the black hole would be smaller because the disc is now viewed under a smaller solid angle. A detailed fully relativistic treatment is needed to examine whether a variation in the corona's position could reproduce the observed trend.

Furthermore, this explanation does not seem to be able to account for the correlation in *SWIFT J0947.6-3057*. The corona flux for this source in 10-40 keV, that is the flux predicted by the power-law model component at this energy range, remains constant over the observation period. If the corona is located closer to the black hole for some of the observations, the corona flux would be expected to decrease, unless a fine tuning between the corona's position and the power-law normalisation is assumed.

Finally, it has been suggested that a varying ionisation level for the disc surface might produce a positive R - Γ correlation. Done & Nayakshin (2001) showed that using a single-ionisation model to fit a reflection spectrum originating from a disc with multiple ionisation layers can produce an apparent correlation. However, the estimated correlation (Fig. 2 in the aforementioned paper) is much weaker than the observed one. The authors also mentioned that a model calculating self-consistently the expected Γ might increase the estimated correlation. It is not easy to conceive why this would be the case though. Instead, it would be expected that variations in the ionised disc surface will result in an anti-correlation between R and Γ . The two authors suggested that an increase in the optical depth of a highly ionised disc surface would result in smaller Γ . At the same time though, increasing the optical depth would increase the albedo of the disc's surface, which will now behave as a mirror for the incident X-rays. This should result in a significant increase of the reflection. As a result, the two parameters would then be anti-correlated.

6. Conclusions

In this work, we studied the NuSTAR spectra of a large sample of nearby Seyfert galaxies. Thanks to the sensitivity of NuSTAR, we studied the reflection hump of these sources in unprecedented detail. Our main findings could be summarised as follows.

The reflection strength was found to be positively correlated with the power-law slope in unabsorbed sources. Such a correlation strongly favours the disc to be the main reflector of the X-ray continuum emission. The same correlation was, also, found for the case of the individual source *SWIFT J0947.6-3057*. Although different mechanisms could, in principle, result in a positive correlation between R and Γ , not all of them were able to reproduce the exact shape of the observed correlation or to explain the large range of observed R values. The most promising explanation is that electrons in the corona are moving with respect to the disc at a moderately relativistic velocity. This model can also explain the existence of the correlation in a single source.

On the other hand, no $R - \Gamma$ correlation was detected in the case of absorbed sources, although both absorbed and unabsorbed sources feature similar levels of reflection. This result might indicate a different origin for the reflection emission of absorbed AGN.

Furthermore, both absorbed and unabsorbed sources were found to exhibit similar luminosity values. Interestingly, the luminosity of individual AGN didn't seem to be driven by the shape of the X-ray spectrum.

Finally, the heavily absorbed sources featured harder spectra than unabsorbed sources. The observed difference in mean Γ between the two groups of objects could be explained if the corona has a slab geometry.

References

Antonucci, R. 1993, *ARA&A*, 31, 473
 Arnaud, K. A. 1996, in *Astronomical Society of the Pacific Conference Series*, Vol. 101, *Astronomical Data Analysis Software and Systems V*, ed. G. H. Jacoby & J. Barnes, 17
 Asplund, M., Grevesse, N., Sauval, A. J., & Scott, P. 2009, *ARA&A*, 47, 481
 Ballantyne, D. R. 2014, *MNRAS*, 437, 2845
 Ballantyne, D. R., Fabian, A. C., & Iwasawa, K. 2004, *MNRAS*, 354, 839
 Baumgartner, W. H., Tueller, J., Markwardt, C. B., et al. 2013, *ApJS*, 207, 19
 Beloborodov, A. M. 1999, *ApJ*, 510, L123
 Brightman, M., Silverman, J. D., Mainieri, V., et al. 2013, *MNRAS*, 433, 2485
 De Marco, B., Ponti, G., Cappi, M., et al. 2013, *MNRAS*, 431, 2441
 Del Moro, A., Alexander, D. M., Aird, J. A., et al. 2017, *ApJ*, 849, 57

Done, C. & Nayakshin, S. 2001, *ApJ*, 546, 419
 Esposito, V. & Walter, R. 2016, *A&A*, 590, A49
 Fabian, A. C., Lohfink, A., Kara, E., et al. 2015, *MNRAS*, 451, 4375
 Fabian, A. C., Zoghbi, A., Ross, R. R., et al. 2009, *Nature*, 459, 540
 Frank, J., King, A., & Raine, D. J. 2002, *Accretion Power in Astrophysics: Third Edition*
 Haardt, F. & Maraschi, L. 1993, *ApJ*, 413, 507
 Harrison, F. A., Craig, W. W., Christensen, F. E., et al. 2013, *ApJ*, 770, 103
 Kara, E., Alston, W. N., Fabian, A. C., et al. 2016, *MNRAS*, 462, 511
 Kara, E., Zoghbi, A., Marinucci, A., et al. 2015, *MNRAS*, 446, 737
 Magdziarz, P. & Zdziarski, A. A. 1995, *MNRAS*, 273, 837
 Malizia, A., Molina, M., Bassani, L., et al. 2014, *ApJ*, 782, L25
 Molina, M., Malizia, A., Bassani, L., et al. 2019, *MNRAS*, 484, 2735
 Mosquera, A. M., Kochanek, C. S., Chen, B., et al. 2013, *ApJ*, 769, 53
 Panagiotou, C. & Walter, R. 2019, *A&A*, 626, A40
 Poutanen, J. & Svensson, R. 1996, *ApJ*, 470, 249
 Poutanen, J., Veledina, A., & Zdziarski, A. A. 2018, *A&A*, 614, A79
 Ricci, C., Trakhtenbrot, B., Koss, M. J., et al. 2017, *ApJS*, 233, 17
 Ricci, C., Walter, R., Courvoisier, T. J.-L., & Paltani, S. 2011, *A&A*, 532, A102
 Saez, C., Chartas, G., Brandt, W. N., et al. 2008, *AJ*, 135, 1505
 Scott, A. E., Stewart, G. C., Mateos, S., et al. 2011, *MNRAS*, 417, 992
 Shakura, N. I. & Sunyaev, R. A. 1973, *A&A*, 500, 33
 Ursini, F., Marinucci, A., Matt, G., et al. 2015, *MNRAS*, 452, 3266
 Vasudevan, R. V., Mushotzky, R. F., & Gandhi, P. 2013, *ApJ*, 770, L37
 Vaughan, S. & Edelson, R. 2001, *ApJ*, 548, 694
 Wang, J.-M. & Zhang, E.-P. 2007, *ApJ*, 660, 1072
 Winter, L. M., Mushotzky, R. F., Reynolds, C. S., & Tueller, J. 2009, *ApJ*, 690, 1322
 Zappacosta, L., Comastri, A., Civano, F., et al. 2018, *ApJ*, 854, 33
 Zdziarski, A. A., Lubiński, P., Gilfanov, M., & Revnivtsev, M. 2003, *MNRAS*, 342, 355
 Zdziarski, A. A., Lubiński, P., & Smith, D. A. 1999, *MNRAS*, 303, L11
 Zoghbi, A., Cackett, E. M., Reynolds, C., et al. 2014, *ApJ*, 789, 56
 Zoghbi, A., Matt, G., Miller, J. M., et al. 2017, *ApJ*, 836, 2

Table 3: Excluded sources

Source Name	Counter part	Exclusion reason
SWIFT J0006.2+2012	Mrk 335	V
SWIFT J0009.4-0037	2MASX J00091156-0036551	F
SWIFT J0025.8+6818	2MASX J00253292+6821442	RD
SWIFT J0101.5-0308	2MASX J01012440-0308399	F
SWIFT J0107.7-1137B	2MASX J01073963-1139117	F
SWIFT J0111.4-3808	NGC 424	RD
SWIFT J0114.4-5522	NGC 454E	RD
SWIFT J0122.8+5003	MCG +08-03-018	RD
SWIFT J0134.1-3625	NGC 612	RD
SWIFT J0201.0-0648	NGC 788	RD
SWIFT J0211.1-4944	ESO 197- G 027	RD
SWIFT J0242.0+0516	2MASX J02420381+0510061	F
SWIFT J0242.6+0000	NGC 1068	RD
SWIFT J0251.3+5441	2MFGC 02280	RD
SWIFT J0255.2-0011	NGC 1142	RD
SWIFT J0304.1-0108	NGC 1194	RD
SWIFT J0308.2-2258	NGC 1229	RD
SWIFT J0317.2+0116	MCG +00-09-042	L
SWIFT J0319.7+4132	NGC 1275	PC
SWIFT J0333.6-3607	NGC 1365	V
SWIFT J0350.1-5019	2MASX J03502377-5018354	F
SWIFT J0357.5-6255	2MASX J03561995-6251391	RD
SWIFT J0359.0-3015A	SARS 059.33488-30.34397	L
SWIFT J0407.4+0339	3C 105	RD
SWIFT J0423.5+0414	2MASX J04234080+0408017	RD
SWIFT J0446.4+1828	UGC 3157	RD
SWIFT J0453.4+0404	CGCG 420-015	RD
SWIFT J0519.5-4545	PICTOR A	L
SWIFT J0601.9-8636	ESO 005- G 004	RD
SWIFT J0615.8+7101	Mrk 3	RD
SWIFT J0632.8+6343	VII Zw 073	F
SWIFT J0651.9+7426	Mrk 6	V
SWIFT J0714.2+3518	MCG +06-16-028	RD
SWIFT J0726.6-3552	2MASX J07262635-3554214	RD
SWIFT J0743.0+6513	Mrk 78	RD
SWIFT J0744.0+2914	UGC 03995A	RD
SWIFT J0756.3-4137	2MASX J07561963-4137420	F
SWIFT J0840.2+2947	4C +29.30	RD
SWIFT J0902.8-7414	2MASX J09034285-7414170	RD
SWIFT J0919.2+5528	SBS 0915+556	F
SWIFT J0924.2-3141	2MASX J09235371-3141305	RD
SWIFT J0935.9+6120	MCG +10-14-025	L
SWIFT J0955.5+6907	M 81	L
SWIFT J1001.7+5543	NGC 3079	RD
SWIFT J1009.3-4250	ESO 263- G 013	RD
SWIFT J1031.7-3451	NGC 3281	RD
SWIFT J1048.4-2511	NGC 3393	RD
SWIFT J1136.7-6007	2MASX J11364205-6003070	L
SWIFT J1157.8+5529	NGC 3998	L
SWIFT J1158.9+4234	IC 0751	V
SWIFT J1203.0+4433	NGC 4051	V
SWIFT J1214.3+2933	Was 49b	RD
SWIFT J1235.6-3954	NGC 4507	RD
SWIFT J1304.3-0532	NGC 4941	RD
SWIFT J1304.3-1022	NGC 4939	RD
SWIFT J1305.4-4928	NGC 4945	RD
SWIFT J1306.4-4025A	ESO 323- G 077	RD

Table 3: Continued.

Source Name	Counter part	Exclusion reason
SWIFT J1309.2+1139	NGC 4992	RD
SWIFT J1322.2-1641	MCG -03-34-064	RD
SWIFT J1333.5-3401	ESO 383- G 018	RD
SWIFT J1355.9+1822	Mrk 463	RD
SWIFT J1416.9-4640	IGR J14175-4641	RD
SWIFT J1424.2+2435	NGC 5610	F
SWIFT J1432.8-4412	NGC 5643	RD
SWIFT J1442.5-1715	NGC 5728	RD
SWIFT J1445.6+2702	CGCG 164-019	F
SWIFT J1508.8-0013	Mrk 1393	V
SWIFT J1630.5+3925	2MASX J16303265+3923031	RD
SWIFT J1631.7+2353	2MASX J16311554+2352577	F
SWIFT J1635.0-5804	ESO 137- G 034	RD
SWIFT J1652.0-5915A	ESO 138- G 001	RD
SWIFT J1652.9+0223	NGC 6240	RD
SWIFT J1719.7+4900	ARP 102B	L
SWIFT J1826.1-0710	1RXS J182557.5-071021	F
SWIFT J1845.4+7211	CGCG 341-006	F
SWIFT J2028.5+2543	MCG +04-48-002	RD
SWIFT J2148.3-3454	NGC 7130	L
SWIFT J2207.3+1013	NGC 7212 NED02	RD
SWIFT J2226.8+3628	MCG +06-49-019	F
SWIFT J2235.9+3358	NGC 7319	RD
SWIFT J2304.9+1220	NGC 7479	L
SWIFT J2318.4-4223	NGC 7582	V

Notes. The first two columns list the Swift BAT name of the source and the name of its counter part. The last column lists the reason for excluding the source from the current analysis; F: low signal-to-noise ratio; L: LINER; RD: reflection dominated spectrum; V: high spectral variability; PC: source in Perseus cluster.

Table 4: Source sample used in this work.

Source Name	Counter part	RA	Dec	z	BAT Class	N_H class
SWIFT J0001.6-7701	Fairall 1203	0.4419	-76.9540	0.0584	4	LOB
SWIFT J0005.0+7021	2MASX J00040192+7019185	1.0082	70.3218	0.0960	5	LOB
SWIFT J0010.5+1057	Mrk 1501	2.6292	10.9749	0.0893	4	UNOB
SWIFT J0034.5-7904	2MASX J00341665-7905204	8.5698	-79.0890	0.0740	4	UNOB
SWIFT J0048.8+3155 [†]	Mrk 348	12.1964	31.9570	0.0150	5	MOB
SWIFT J0051.9+1724	Mrk 1148	12.9782	17.4329	0.0640	4	UNOB
SWIFT J0100.9-4750	ESO 195-IG 021 NED03	15.1457	-47.8676	0.0483	5	UNOB
SWIFT J0105.6-3433	HE 0103-3447	16.4442	-34.5292	0.0570	4	UNOB
SWIFT J0114.5-3236	IC 1657	18.5293	-32.6509	0.0120	5	MOB
SWIFT J0123.9-5846	Fairall 9	20.9407	-58.8058	0.0470	4	UNOB
SWIFT J0124.5+3350	NGC 513	21.1119	33.7994	0.0195	5	LOB
SWIFT J0128.0-1850	MCG -03-04-072	22.0279	-18.8085	0.0460	4	UNOB
SWIFT J0140.6-5321	2MASX J01402676-5319389	25.1116	-53.3276	0.0716	5	LOB
SWIFT J0152.8-0329 [†]	MCG -01-05-047	28.2042	-3.4468	0.0172	5	MOB
SWIFT J0155.4+0228	1ES 0152+022	28.8538	2.4712	0.0820	4	UNOB
SWIFT J0206.2-0019	Mrk 1018	31.5666	-0.2914	0.0424	4	UNOB
SWIFT J0214.6-0049 [†]	Mrk 590	33.6398	-0.7666	0.0264	4	UNOB
SWIFT J0214.9-6432	2MASX J02143730-6430052	33.6557	-64.5014	0.0740	4	UNOB
SWIFT J0226.4-2821	AM 0224-283	36.6081	-28.3503	0.0598	4	UNOB
SWIFT J0228.1+3118 [†]	NGC 931	37.0603	31.3117	0.0167	4	UNOB
SWIFT J0230.2-0900	Mrk 1044	37.5230	-8.9981	0.0165	4	UNOB
SWIFT J0234.6-0848 [†]	NGC 985	38.6574	-8.7876	0.0431	4	LOB
SWIFT J0235.3-2934	ESO 416- G 002	38.8061	-29.6047	0.0591	5	UNOB
SWIFT J0241.3-0816	NGC 1052	40.2700	-8.2558	0.0050	5	MOB

Table 4: Continued.

Source Name	Counter part	RA	Dec	z	BAT Class	N_H class
SWIFT J0241.6+0711	Mrk 595	40.3954	7.1872	0.0270	4	LOB
SWIFT J0244.8+6227	[HB89] 0241+622	41.2404	62.4685	0.0440	4	UNOB
SWIFT J0308.5-7251	ESO 031- G 008	46.8972	-72.8340	0.0276	4	UNOB
SWIFT J0318.7+6828 [†]	2MASX J03181899+6829322	49.5791	68.4921	0.0901	5	LOB
SWIFT J0324.8+3410 [†]	1H 0323+342	51.1715	34.1794	0.0610	4	UNOB
SWIFT J0325.0-4154	LCRS B032315.2-420449	51.2593	-41.9049	0.0580	4	UNOB
SWIFT J0347.0-3027	1RXS J034704.9-302409	56.7726	-30.3975	0.0950	4	UNOB
SWIFT J0356.9-4041	2MASX J03565655-4041453	59.2356	-40.6960	0.0748	5	LOB
SWIFT J0418.3+3800	3C 111.0	64.5887	38.0266	0.0485	4	UNOB
SWIFT J0426.2-5711	1H 0419-577	66.5030	-57.2003	0.1040	5	UNOB
SWIFT J0433.0+0521	3C 120	68.2962	5.3543	0.0330	4	UNOB
SWIFT J0437.4-4713	2MASX J04372814-4711298	69.3673	-47.1915	0.0530	4	UNOB
SWIFT J0441.2-2704	IRAS 04392-2713	70.3440	-27.1386	0.0835	4	UNOB
SWIFT J0456.3-7532 [†]	ESO 033- G 002	73.9957	-75.5412	0.0181	5	UNOB
SWIFT J0501.9-3239	ESO 362- G 018	79.8992	-32.6576	0.0124	4	UNOB
SWIFT J0504.6-7345	2MASX J05043414-7349269	76.1425	-73.8242	0.0452	5	UNOB
SWIFT J0505.8-2351 [†]	2MASX J05054575-2351139	76.4405	-23.8539	0.0350	5	MOB
SWIFT J0508.1+1727	CGCG 468-002 NED01	77.0820	17.3634	0.0175	5	UNOB
SWIFT J0516.2-0009	Ark 120	79.0476	-0.1498	0.0327	4	
SWIFT J0521.0-2522	2MASX J05210136-2521450	80.2558	-25.3626	0.0426	5	LOB
SWIFT J0526.2-2118	ESO 553- G 043	81.6135	-21.2866	0.0278	5	MOB
SWIFT J0552.2-0727 [†]	NGC 2110	88.0474	-7.4562	0.0078	5	LOB
SWIFT J0554.8+4625	MCG +08-11-011	88.7234	46.4393	0.0205	4	UNOB
SWIFT J0623.3-6438	2MASX J06230765-6436211	95.7821	-64.6057	0.1289	4	UNOB
SWIFT J0623.8+6445	NVSS J062335+644538	95.8964	64.7601	0.0860	4	UNOB
SWIFT J0623.9-6058 [†]	ESO 121-IG 028	95.9399	-60.9790	0.0405	5	MOB
SWIFT J0640.1-4328	2MASX J06403799-4321211	100.1583	-43.3558	0.0610	5	MOB
SWIFT J0641.3+3257	2MASX J06411806+3249313	100.3252	32.8254	0.0470	5	MOB
SWIFT J0655.8+3957	UGC 03601	103.9564	40.0002	0.0171	4	UNOB
SWIFT J0709.0-4642	2MASX J07084326-4642494	107.1803	-46.7137	0.0469	5	LOB
SWIFT J0714.3+4541	Mrk 376	108.5628	45.6988	0.0560	4	UNOB
SWIFT J0736.9+5846	Mrk 9	114.2374	58.7704	0.0399	4	UNOB
SWIFT J0739.7-3142	2MASX J07394469-3143024	114.9362	-31.7174	0.0258	5	MOB
SWIFT J0742.3+8024	3C 184.1	115.7557	80.4406	0.1182	4	MOB
SWIFT J0804.2+0507	Mrk 1210	121.0244	5.1138	0.0135	5	MOB
SWIFT J0804.6+1045	MCG +02-21-013	121.1933	10.7767	0.0344	4	MOB
SWIFT J0810.9+7602 [†]	PG 0804+761	122.7442	76.0451	0.1000	4	UNOB
SWIFT J0823.4-0457	Fairall 272	125.7546	-4.9349	0.0218	5	MOB
SWIFT J0838.4-3557 [†]	Fairall 1146	129.6283	-35.9926	0.0316	4	UNOB
SWIFT J0843.5+3551	2MASX J08434495+3549421	130.9375	35.8283	0.0540	5	MOB
SWIFT J0855.6+6425	MCG +11-11-032	133.8023	64.3960	0.0363	5	MOB
SWIFT J0856.0+7812	NGC 2655	133.9072	78.2231	0.0047	5	MOB
SWIFT J0902.0+6007	Mrk 18	135.4933	60.1517	0.0111	5	MOB
SWIFT J0911.2+4533	2MASX J09112999+4528060	137.8749	45.4683	0.0268	5	MOB
SWIFT J0917.2-6221	IRAS 09149-6206	139.0391	-62.3250	0.0573	4	UNOB
SWIFT J0918.5+1618	Mrk 704	139.6084	16.3053	0.0292	4	LOB
SWIFT J0920.1+3712	IC 2461	139.9918	37.1913	0.0075	5	LOB
SWIFT J0920.8-0805 [†]	MCG -01-24-012	140.1927	-8.0561	0.0196	5	LOB
SWIFT J0923.7+2255	MCG +04-22-042	140.9292	22.9091	0.0324	4	UNOB
SWIFT J0925.0+5218	Mrk 110	141.3036	52.2863	0.0353	4	UNOB
SWIFT J0925.2-8423	2MASX J09261742-8421330	141.5735	-84.3593	0.0632	5	UNOB
SWIFT J0926.1+6931 [†]	2MASX J09254750+6927532	141.4481	69.4648	0.0398	4	MOB
SWIFT J0945.6-1420 [†]	NGC 2992	146.4252	-14.3264	0.0077	5	UNOB
SWIFT J0947.6-3057	MCG -05-23-016	146.9173	-30.9487	0.0085	5	
SWIFT J0947.7+0726	3C 227	146.9382	7.4223	0.0863	4	UNOB
SWIFT J1021.7-0327	ARK 241	155.4177	-3.4539	0.0408	4	UNOB
SWIFT J1023.5+1952	NGC 3227	155.8774	19.8651	0.0039	4	
SWIFT J1043.4+1105	SDSS J104326.47+110524.2	160.8603	11.0901	0.0477	4	UNOB

Table 4: Continued.

Source Name	Counter part	RA	Dec	z	BAT Class	N_H class
SWIFT J1044.1+7024	MCG +12-10-067	161.0356	70.4054	0.0336	5	MOB
SWIFT J1044.8+3812	MCG +06-24-008	161.2040	38.1810	0.0259	5	LOB
SWIFT J1046.8+2556	UGC 05881	161.6772	25.9316	0.0206	5	MOB
SWIFT J1049.4+2258 [†]	Mrk 417	162.3789	22.9646	0.0328	5	MOB
SWIFT J1052.8+1043	2MASX J10523297+1036205	163.1374	10.6056	0.0878	4	LOB
SWIFT J1059.8+6507	2MASX J10594361+6504063	164.9315	65.0684	0.0836	5	LOB
SWIFT J1100.9+1104	Mrk 728	165.2574	11.0469	0.0357	5	UNOB
SWIFT J1105.7+5854A	CGCG 291-028	166.4959	58.9460	0.0477	5	MOB
SWIFT J1106.5+7234	NGC 3516	166.6979	72.5686	0.0088	4	UNOB
SWIFT J1110.6-2832	ESO 438- G 009	167.7000	-28.5011	0.0240	4	UNOB
SWIFT J1113.6+0936	IC 2637	168.4573	9.5863	0.0292	4	UNOB
SWIFT J1136.0+2132	Mrk 739E	174.1224	21.5960	0.0297	4	UNOB
SWIFT J1139.0-3743	NGC 3783	174.7573	-37.7387	0.0097	4	
SWIFT J1139.1+5913	SBS 1136+594	174.7873	59.1985	0.0601	4	UNOB
SWIFT J1139.8+3157	NGC 3786	174.9273	31.9093	0.0089	5	LOB
SWIFT J1142.2+1021	NGC 3822	175.5463	10.2778	0.0209	5	UNOB
SWIFT J1143.7+7942	UGC 06728	176.3168	79.6815	0.0065	4	UNOB
SWIFT J1145.6-1819	2MASX J11454045-1827149	176.4186	-18.4543	0.0330	4	UNOB
SWIFT J1149.3-0414	2MASX J11491868-0416512	177.3278	-4.2808	0.0845	4	UNOB
SWIFT J1152.6-0512	MCG -01-30-041	178.1590	-5.2071	0.0188	5	UNOB
SWIFT J1201.2-0341	Mrk 1310	180.3098	-3.6781	0.0196	4	UNOB
SWIFT J1202.5+3332 [†]	NGC 4395	186.4536	33.5469	0.0011	5	UNOB
SWIFT J1205.8+4959	2MASX J12055599+4959561	181.4834	49.9990	0.0631	5	UNOB
SWIFT J1207.5+3355	B2 1204+34	181.8871	33.8778	0.0791	5	LOB
SWIFT J1210.1-4637	2MASX J12100404-4636274	182.5168	-46.6076	0.0315	5	UNOB
SWIFT J1210.5+3924	NGC 4151	182.6357	39.4057	0.0033	4	
SWIFT J1217.2-2611	ESO 505-IG 030	184.2380	-26.2093	0.0397	5	MOB
SWIFT J1218.5+2952 [†]	Mrk 766	184.6105	29.8129	0.0129	4	UNOB
SWIFT J1219.4+4720 [†]	M 106	184.7396	47.3040	0.0015	5	MOB
SWIFT J1225.8+1240	NGC 4388	186.4448	12.6621	0.0084	5	MOB
SWIFT J1232.0-4802	2MASX J12313717-4758019	187.9048	-47.9672	0.0277	4	UNOB
SWIFT J1232.1+2009	Mrk 771	188.0150	20.1581	0.0630	4	UNOB
SWIFT J1239.3-1611 [†]	LEDA 170194	189.7762	-16.1797	0.0367	5	LOB
SWIFT J1239.6-0519 [†]	NGC 4593	189.9143	-5.3443	0.0090	4	UNOB
SWIFT J1241.6-5748 [†]	WKK 1263	190.3573	-57.8343	0.0244	4	UNOB
SWIFT J1255.0-2657	6dF J1254564-265702	193.7349	-26.9506	0.0591	5	UNOB
SWIFT J1315.8+4420	UGC 08327 NED02	198.8219	44.4071	0.0366	5	LOB
SWIFT J1325.4-4301	Cen A	201.3651	-43.0191	0.0018	5	MOB
SWIFT J1331.2-2524	ESO 509- G 038	202.8079	-25.4028	0.0260	4	UNOB
SWIFT J1334.8-2328	ESO 509-IG 066	203.6667	-23.4464	0.0343	5	LOB
SWIFT J1335.8-3416 [†]	MCG -06-30-015	203.9738	-34.2955	0.0078	4	UNOB
SWIFT J1338.2+0433 [†]	NGC 5252	204.5665	4.5426	0.0230	5	LOB
SWIFT J1341.5+6742	NGC 5283	205.2740	67.6723	0.0104	5	MOB
SWIFT J1341.9+3537	NGC 5273	205.5347	35.6542	0.0036	5	UNOB
SWIFT J1347.4-6033	4U 1344-60	206.8998	-60.6177	0.0129	4	UNOB
SWIFT J1349.3-3018	IC 4329A	207.3303	-30.3094	0.0161	4	UNOB
SWIFT J1349.7+0209	UM 614	207.4702	2.0792	0.0327	4	UNOB
SWIFT J1354.5+1326	2MASX J13542913+1328068	208.6216	13.4687	0.0635	5	MOB
SWIFT J1410.9-4229	2MASX J14104482-4228325	212.6868	-42.4758	0.0339	5	LOB
SWIFT J1413.2-0312 [†]	NGC 5506	213.3121	-3.2076	0.0062	5	UNOB
SWIFT J1417.9+2507	NGC 5548	214.4981	25.1368	0.0172	4	
SWIFT J1427.5+1949	Mrk 813	216.8544	19.8310	0.1105	4	UNOB
SWIFT J1429.2+0118	Mrk 1383	217.2775	1.2851	0.0866	4	UNOB
SWIFT J1433.9+0528	NGC 5674	218.4677	5.4582	0.0249	5	LOB
SWIFT J1436.4+5846	Mrk 817	219.0919	58.7943	0.0315	4	UNOB
SWIFT J1441.4+5341 [†]	Mrk 477	220.1587	53.5044	0.0377	4	MOB
SWIFT J1446.7-6416 [†]	IGR J14471-6414	221.6164	-64.2731	0.0530	4	UNOB
SWIFT J1454.9-5133 [†]	WKK 4438	223.8242	-51.5714	0.0160	4	UNOB

Table 4: Continued.

Source Name	Counter part	RA	Dec	z	BAT Class	N_H class
SWIFT J1457.8-4308 [†]	IC 4518A	224.4288	-43.1317	0.0157	5	MOB
SWIFT J1504.2+1025 [†]	Mrk 841	226.0050	10.4378	0.0364	4	UNOB
SWIFT J1506.7+0353A	Mrk 1392	226.4856	3.7073	0.0361	4	UNOB
SWIFT J1506.7+0353B	2MASX J15064412+0351444	226.6839	3.8623	0.0373	5	UNOB
SWIFT J1513.8-8125	2MASX J15144217-8123377	228.6751	-81.3939	0.0684	4	LOB
SWIFT J1515.0+4205	NGC 5899	228.7634	42.0498	0.0085	5	MOB
SWIFT J1519.6+6538	CGCG 319-007	229.8904	65.5996	0.0440	5	MOB
SWIFT J1530.0-1300	2MASX J15295830-1300397	232.4930	-13.0110	0.1039	4	UNOB
SWIFT J1533.2-0836	MCG -01-40-001	233.3363	-8.7005	0.0227	5	LOB
SWIFT J1535.9+5751	Mrk 290	233.9682	57.9026	0.0296	4	UNOB
SWIFT J1548.5-1344 [†]	NGC 5995	237.1040	-13.7578	0.0252	5	UNOB
SWIFT J1557.8-7913	PKS 1549-79	239.2453	-79.2345	0.1522	4	LOB
SWIFT J1613.2-6043	WKK 6092	242.9642	-60.6319	0.0156	4	UNOB
SWIFT J1621.2+8104	CGCG 367-009	244.8302	81.0465	0.0239	5	MOB
SWIFT J1626.7+8530	VII Zw 653	246.3580	85.4949	0.0631	4	UNOB
SWIFT J1628.1+5145	Mrk 1498	247.0169	51.7754	0.0547	5	MOB
SWIFT J1648.0-3037 [†]	2MASX J16481523-3035037	252.0635	-30.5845	0.0310	4	UNOB
SWIFT J1650.5+0434 [†]	LEDA 214543	252.6781	4.6050	0.0320	5	UNOB
SWIFT J1717.1-6249 [†]	NGC 6300	259.2478	-62.8206	0.0037	5	MOB
SWIFT J1737.5-2908	AX J1737.4-2907	264.3681	-29.1340	0.0214	4	UNOB
SWIFT J1741.9-1211	2E 1739.1-1210	265.4803	-12.1991	0.0370	4	UNOB
SWIFT J1745.4+2906	1RXS J174538.1+290823	266.4094	29.1395	0.1113	4	LOB
SWIFT J1748.8-3257	2MASS J17485512-3254521	267.2297	-32.9145	0.0200	4	UNOB
SWIFT J1802.8-1455 [†]	2MASXi J1802473-145454	270.6896	-14.9089	0.0350	4	UNOB
SWIFT J1816.0+4236	UGC 11185 NED02	274.0481	42.6603	0.0412	5	LOB
SWIFT J1824.2+1845	2MASX J18241083+1846088	276.0451	18.7691	0.0670	5	MOB
SWIFT J1824.3-5624 [†]	IC 4709	276.0808	-56.3692	0.0169	5	MOB
SWIFT J1826.8+3254	2MASX J18263239+3251300	276.6350	32.8583	0.0220	5	MOB
SWIFT J1830.8+0928	2MASX J18305065+0928414	277.7110	9.4783	0.0194	5	MOB
SWIFT J1835.0+3240	3C 382	278.7641	32.6963	0.0579	4	UNOB
SWIFT J1836.9-5924	Fairall 49	279.2429	-59.4024	0.0200	5	UNOB
SWIFT J1838.4-6524	ESO 103- G 035	279.5848	-65.4276	0.0133	5	MOB
SWIFT J1842.0+7945	3C 390.3	280.5375	79.7714	0.0561	4	UNOB
SWIFT J1856.1+1539	2MASX J18560128+1538059	284.0053	15.6349	0.0840	4	LOB
SWIFT J1856.2-7829	2MASX J18570768-7828212	284.2823	-78.4726	0.0420	4	UNOB
SWIFT J1905.4+4231	CGCG 229-015	286.3581	42.4610	0.0279	4	UNOB
SWIFT J1913.3-5010	ESO 231- G 026	288.3115	-50.1829	0.0625	5	MOB
SWIFT J1921.1-5842 [†]	ESO 141- G 055	290.3089	-58.6703	0.0371	4	UNOB
SWIFT J1926.9+4140	2MASX J19263018+4133053	291.6258	41.5514	0.0720	5	UNOB
SWIFT J1930.5+3414	2MASX J19301380+3410495	292.5554	34.1797	0.0629	4	MOB
SWIFT J1933.9+3258 [†]	2MASS J19334715+3254259	293.4465	32.9072	0.0565	4	UNOB
SWIFT J1937.5-0613 [†]	2MASX J19373299-0613046	294.3875	-6.2180	0.0102	4	UNOB
SWIFT J1938.1-5108	2MASX J19380437-5109497	294.5183	-51.1638	0.0400	4	UNOB
SWIFT J1942.6-1024 [†]	NGC 6814	295.6694	-10.3235	0.0052	4	UNOB
SWIFT J1947.3+4447 [†]	2MASX J19471938+4449425	296.8307	44.8284	0.0539	5	MOB
SWIFT J1952.4+0237	3C 403	298.0659	2.5067	0.0590	5	MOB
SWIFT J2001.0-1811	2MASX J20005575-1810274	300.2321	-18.1743	0.0371	4	LOB
SWIFT J2006.5+5619	2MASX J20063331+5620364	301.6389	56.3435	0.0430	5	MOB
SWIFT J2018.8+4041	2MASX J20183871+4041003	304.6613	40.6834	0.0144	5	MOB
SWIFT J2021.9+4400 [†]	2MASX J20214907+4400399	305.4544	44.0110	0.0170	5	LOB
SWIFT J2035.2+2604	2MASX J20350566+2603301	308.7735	26.0583	0.0500	4	UNOB
SWIFT J2044.2-1045 [†]	Mrk 509	311.0406	-10.7235	0.0344	4	UNOB
SWIFT J2052.0-5704	IC 5063	313.0098	-57.0688	0.0114	5	MOB
SWIFT J2114.4+8206	2MASX J21140128+8204483	318.5049	82.0801	0.0840	4	UNOB
SWIFT J2118.9+3336 [†]	2MASX J21192912+3332566	319.8675	33.5514	0.0510	5	UNOB
SWIFT J2127.4+5654 [†]	SWIFT J212745.6+565636	321.9372	56.9443	0.0144	4	UNOB

Table 4: Continued.

Source Name	Counter part	RA	Dec	z	BAT Class	N_H class
SWIFT J2134.9-2729	2MASX J21344509-2725557	323.6880	-27.4321	0.0690	4	UNOB
SWIFT J2200.9+1032 [†]	Mrk 520	330.1746	10.5497	0.0266	5	UNOB
SWIFT J2201.9-3152 [†]	NGC 7172	330.5079	-31.8697	0.0087	5	MOB
SWIFT J2209.4-4711	NGC 7213	332.3180	-47.1666	0.0058	4	UNOB
SWIFT J2211.7+1843	II Zw 171	332.9745	18.6972	0.0700	4	UNOB
SWIFT J2223.9-0207	3C 445	335.9564	-2.1036	0.0559	5	MOB
SWIFT J2235.9-2602 [†]	NGC 7314	338.9425	-26.0505	0.0048	5	UNOB
SWIFT J2236.7-1233	Mrk 915	339.1938	-12.5452	0.0241	4	
SWIFT J2240.2+0801	MCG +01-57-016	340.0710	8.0539	0.0250	5	UNOB
SWIFT J2246.0+3941	3C 452	341.4532	39.6878	0.0811	5	MOB
SWIFT J2301.4-5916	2MASX J23013626-5913210	345.4010	-59.2225	0.1501	4	UNOB
SWIFT J2303.3+0852 [†]	NGC 7469	345.8151	8.8740	0.0163	4	UNOB
SWIFT J2304.8-0843	Mrk 926	346.1812	-8.6857	0.0469	4	UNOB
SWIFT J2325.5-3827	LCRS B232242.2-384320	351.3508	-38.4470	0.0359	4	UNOB
SWIFT J2328.9+0328	NGC 7679	352.1946	3.5115	0.0171	5	UNOB
SWIFT J2330.5+7124 [†]	IGR J23308+7120	352.6570	71.3796	0.0370	5	LOB
SWIFT J2333.9-2342	PKS 2331-240	353.4802	-23.7280	0.0477	5	UNOB
SWIFT J2359.3-6058	PKS 2356-61	359.7682	-60.9165	0.0963	5	MOB

Notes. The name and counter part of each source, its celestial coordinates as well as its BAT class, are as given in the BAT catalogue. The redshift was retrieved by NED (<https://ned.ipac.caltech.edu/>) and SIMBAD (<http://simbad.u-strasbg.fr/simbad/>). The last column lists the N_H based classification of each object. We have defined three groups; the unobscured ($N_H < 5 \cdot 10^{22} \text{ cm}^{-2}$, UNOB), the lightly obscured ($5 \cdot 10^{22} \text{ cm}^{-2} < N_H < 10^{23} \text{ cm}^{-2}$, LOB) and the mildly obscured ($N_H > 10^{23} \text{ cm}^{-2}$, MOB) class. Sources with moderate spectral variability have not been considered in this classification.

Table 5: Observation log of the used sample.

Source Name	NuSTAR Obs ID	Obs date (MJD)	Exposure (ks)
SWIFT J0001.6-7701	60160002002	57123.549	33.91
SWIFT J0005.0+7021	60061001002	58463.427	23.60
SWIFT J0010.5+1057	60301014002	58098.661	73.05
SWIFT J0034.5-7904	60160015002	57475.793	22.60
SWIFT J0048.8+3155	60160026002	57323.296	21.52
SWIFT J0051.9+1724	60160028002	58132.618	17.17
SWIFT J0100.9-4750	60061344002	56882.288	22.78
SWIFT J0105.6-3433	60160038002	58521.145	18.88
SWIFT J0114.5-3236	60061008002	56318.624	2.41
	60061008003	56318.683	9.99
	60261007002	57769.001	36.30
SWIFT J0123.9-5846	60001130002	56786.095	49.21
	60001130003	56786.969	93.30
SWIFT J0124.5+3350	60061012002	56339.297	16.04
SWIFT J0128.0-1850	60160061002	57034.265	21.88
SWIFT J0140.6-5321	60160072002	57084.473	22.56
SWIFT J0152.8-0329	60061016002	56261.015	13.42
SWIFT J0155.4+0228	60160080002	58064.292	21.01
SWIFT J0206.2-0019	60160087002	57428.939	21.62
	60301022002	58123.560	26.92
	60301022003	58182.021	43.43
SWIFT J0214.6-0049	60160095002	57423.702	21.21
	90201043002	57724.495	50.62
SWIFT J0214.9-6432	60061021002	57767.595	23.08
SWIFT J0226.4-2821	60363002002	57921.786	22.06
SWIFT J0228.1+3118	60101002002	57246.997	50.03
	60101002004	57249.208	49.75
SWIFT J0230.2-0900	60160109002	57426.322	21.68
SWIFT J0234.6-0848	60061025002	56515.496	13.89
SWIFT J0235.3-2934	60061340002	57030.839	20.32
SWIFT J0241.3-0816	60061027002	56337.416	15.58
	60201056002	57770.012	47.03

Table 5: Continued.

Source Name	NuSTAR Obs ID	Obs date (MJD)	Exposure (ks)
SWIFT J0241.6+0711	60160119002	57771.355	21.30
SWIFT J0244.8+6227	60160125002	57600.282	22.12
SWIFT J0308.5-7251	60160141002	57866.654	25.05
SWIFT J0318.7+6828	60061342002	57512.802	24.04
SWIFT J0324.8+3410	60061360002	56731.742	100.95
SWIFT J0325.0-4154	60160152002	57374.278	21.86
SWIFT J0347.0-3027	60061039002	56366.789	6.36
	60061039004	56375.142	12.70
	60061039006	56384.506	9.52
	60376003002	58413.233	52.21
SWIFT J0356.9-4041	60061341002	57126.007	21.90
SWIFT J0418.3+3800	60202061002	58113.708	15.34
	60202061004	58116.116	49.13
SWIFT J0426.2-5711	60101039002	57176.795	168.58
SWIFT J0433.0+0521	60001042002	56329.539	21.61
	60001042003	56330.011	127.49
SWIFT J0437.4-4713	30001061002	57020.626	73.03
	30001061004	57022.780	63.87
	30001061006	57024.727	63.14
	60160197002	57365.751	19.75
SWIFT J0441.2-2704	60160201002	57376.974	13.94
SWIFT J0456.3-7532	60061054002	56781.032	23.04
SWIFT J0501.9-3239	60201046002	57655.824	100.22
SWIFT J0504.6-7345	60160217002	57661.563	22.19
SWIFT J0505.8-2351	60061056002	56525.403	21.16
SWIFT J0508.1+1727	60006011002	56131.910	15.52
SWIFT J0516.2-0009	60001044002	56341.465	55.24
	60001044004	56738.410	64.70
SWIFT J0521.0-2522	60002027002	56343.419	22.89
	60002027004	56567.422	19.13
	60002027005	56567.965	7.88
	60201022002	57636.151	129.75
SWIFT J0526.2-2118	60160236002	57616.345	21.51
SWIFT J0552.2-0727	60061061002	56205.233	15.54
	60061061004	56337.088	11.51
SWIFT J0554.8+4625	60201027002	57616.815	78.11
SWIFT J0623.3-6438	60160263002	58010.862	32.27
SWIFT J0623.8+6445	60376012002	58433.638	47.60
SWIFT J0623.9-6058	60061065002	56877.124	20.21
SWIFT J0640.1-4328	60061070002	56678.044	18.66
SWIFT J0641.3+3257	60061071002	58483.913	17.11
SWIFT J0655.8+3957	60160278002	58489.081	15.59
SWIFT J0709.0-4642	60160284002	57221.746	25.19
SWIFT J0714.3+4541	60160288002	57119.834	23.81
SWIFT J0736.9+5846	60061326002	56594.357	23.20
SWIFT J0739.7-3142	60061351002	56767.954	22.34
SWIFT J0742.3+8024	60160300002	57296.421	21.78
SWIFT J0804.2+0507	60061078002	56205.644	15.45
SWIFT J0804.6+1045	60260001002	57823.598	20.34
SWIFT J0810.9+7602	60160322002	57480.117	16.94
SWIFT J0823.4-0457	60061080002	56667.343	22.90
SWIFT J0838.4-3557	60061082002	56865.966	21.28
SWIFT J0843.5+3551	60260002002	57753.780	14.68
SWIFT J0855.6+6425	60061086002	57436.813	4.32
SWIFT J0856.0+7812	60160341002	57694.891	5.09
	60160341004	57702.685	15.53
SWIFT J0902.0+6007	60061088002	56641.220	19.80
SWIFT J0911.2+4533	60061089002	57015.010	14.99

Table 5: Continued.

Source Name	NuSTAR Obs ID	Obs date (MJD)	Exposure (ks)
SWIFT J0917.2-6221	90401630002	58361.030	111.72
SWIFT J0918.5+1618	60061090002	57019.562	21.52
SWIFT J0920.1+3712	60061353002	56821.979	32.78
SWIFT J0920.8-0805	60061091002	56385.532	12.38
	60061091004	56392.605	9.39
	60061091006	56400.693	11.59
	60061091008	56417.729	14.09
	60061091010	56424.532	15.33
	60061091012	56434.298	12.29
SWIFT J0923.7+2255	60061092002	56287.578	18.85
SWIFT J0925.0+5218	60201025002	57776.808	152.43
SWIFT J0925.2-8423	60160360002	57356.201	35.13
SWIFT J0926.1+6931	60201030002	57569.884	44.10
SWIFT J0945.6-1420	60160371002	57358.578	20.80
SWIFT J0947.6-3057	10002019001	56119.999	32.88
	60001046002	56446.354	157.43
	60001046004	57068.498	208.38
	60001046006	57074.010	96.78
	60001046008	57094.779	215.95
SWIFT J0947.7+0726	60061329002	56708.812	16.63
	60061329004	56714.061	12.06
SWIFT J1021.7-0327	60160392002	58109.082	20.18
SWIFT J1023.5+1952	60202002002	57701.555	49.80
	60202002004	57717.398	34.55
	60202002006	57721.695	38.91
	60202002008	57723.440	40.58
	60202002010	57727.401	40.23
	60202002012	57731.362	30.98
	60202002014	57774.998	45.52
SWIFT J1043.4+1105	60160406002	57553.665	13.20
SWIFT J1044.1+7024	60061204002	57037.459	24.14
SWIFT J1044.8+3812	60061359002	56963.830	24.11
SWIFT J1046.8+2556	60160409002	57159.217	21.41
SWIFT J1049.4+2258	60061206002	57804.539	20.69
SWIFT J1052.8+1043	60160414002	57784.012	32.93
SWIFT J1059.8+6507	60061207002	58423.914	26.05
SWIFT J1100.9+1104	60061338002	56705.784	23.24
SWIFT J1105.7+5854A	60160420002	58568.617	15.77
SWIFT J1106.5+7234	60002042002	56832.702	50.42
	60002042004	56849.634	71.33
	60302016002	58092.703	23.02
	60302016004	58094.716	31.20
	60302016006	58098.010	32.57
	60302016008	58113.236	21.83
	60302016010	58115.452	33.80
	60302016012	58117.197	27.20
SWIFT J1110.6-2832	60160423002	57054.998	21.45
SWIFT J1113.6+0936	60061208002	56454.658	21.42
SWIFT J1136.0+2132	60260008002	57828.171	18.31
SWIFT J1139.0-3743	60101110002	57622.274	40.08
	60101110004	57624.892	40.74
	80202006002	57733.916	18.77
	80202006004	57743.448	23.20
SWIFT J1139.1+5913	60160443002	57017.681	23.53
SWIFT J1139.8+3157	60061349002	56817.613	21.80
SWIFT J1142.2+1021	60061332002	57399.415	18.86
SWIFT J1143.7+7942	60160450002	57579.484	21.20
	60376007002	58039.838	45.44

Table 5: Continued.

Source Name	NuSTAR Obs ID	Obs date (MJD)	Exposure (ks)
SWIFT J1145.6-1819	60302002002	58103.515	20.76
	60302002004	58105.529	19.19
	60302002006	58107.408	22.65
	60302002008	58109.556	20.59
	60302002010	58111.570	22.10
SWIFT J1149.3-0414	60061215002	57786.146	31.88
SWIFT J1152.6-0512	60061216002	57918.192	26.66
SWIFT J1201.2-0341	60160465002	57556.544	21.13
SWIFT J1202.5+3332	60061322002	56422.114	18.95
SWIFT J1205.8+4959	60061357002	56953.814	22.43
SWIFT J1207.5+3355	60301012002	58077.336	39.60
	60061356002	57007.335	18.83
	60061345002	56805.035	19.85
	60001111002	56243.264	21.86
	60001111003	56243.792	57.04
SWIFT J1210.5+3924	60001111005	56245.345	60.53
	60061226002	58146.741	21.48
	60001048002	57046.525	89.36
SWIFT J1217.2-2611	60101022002	57208.740	16.30
	60101046002	57342.466	53.00
	60101046004	57397.133	102.08
SWIFT J1225.8+1240	60061228002	56653.285	19.86
SWIFT J1232.0-4802	60160498002	57621.806	18.28
SWIFT J1232.1+2009	60061229002	57597.444	14.32
SWIFT J1239.3-1611	60061232002	57402.305	21.35
SWIFT J1239.6-0519	60001149002	57020.042	22.10
	60001149004	57022.193	20.79
	60001149006	57024.143	20.56
	60001149008	57026.092	22.10
	60001149010	57028.646	21.14
SWIFT J1241.6-5748	60160510002	57505.853	16.37
SWIFT J1255.0-2657	60363001002	57929.740	19.30
SWIFT J1315.8+4420	60061241002	56403.870	12.60
	60061241004	56613.970	28.91
	60061241006	56619.422	22.60
	60363006002	58072.910	19.33
	60001081002	56510.547	51.26
SWIFT J1325.4-4301	60101063002	57159.697	21.73
	60466005002	58231.180	17.35
	60260010002	57520.963	19.44
SWIFT J1331.2-2524	60061244002	56902.979	20.93
SWIFT J1334.8-2328	60001047002	56321.478	23.27
	60001047003	56322.016	125.86
	60001047005	56325.452	29.49
	60061245002	56423.072	19.01
	60465006002	58439.632	32.69
SWIFT J1341.5+6742	60061350002	56852.129	21.12
SWIFT J1341.9+3537	60201041002	57648.396	99.02
SWIFT J1347.4-6033	60001045002	56151.683	162.40
SWIFT J1349.3-3018	60160560002	57112.862	18.20
SWIFT J1349.7+0209	60160565002	58556.768	19.58
SWIFT J1354.5+1326	60160571002	57156.472	22.04
SWIFT J1410.9-4229	60061323002	56748.996	56.59
SWIFT J1413.2-0312	60002044002	56484.419	22.77
	60002044003	56485.026	26.96
	60002044005	56496.613	49.39
	60002044006	56545.904	51.11
	60002044008	56646.357	50.10
SWIFT J1417.9+2507	60160583002	57776.169	18.50

Table 5: Continued.

Source Name	NuSTAR Obs ID	Obs date (MJD)	Exposure (ks)
SWIFT J1429.2+0118	60061254002	58340.381	32.48
SWIFT J1433.9+0528	60061337002	56848.634	20.49
SWIFT J1436.4+5846	60160590002	57228.489	20.53
SWIFT J1441.4+5341	60061255002	56792.194	18.08
	60061255004	56801.208	16.80
SWIFT J1446.7-6416	60061257002	56440.318	15.04
SWIFT J1454.9-5133	60061259002	56554.660	21.90
SWIFT J1457.8-4308	60061260002	56506.510	7.79
SWIFT J1504.2+1025	60101023002	57217.742	17.70
SWIFT J1506.7+0353A	60160605002	58143.863	15.94
SWIFT J1506.7+0353B	60061261002	56908.364	21.32
	60301023002	58138.031	50.58
SWIFT J1513.8-8125	60061263002	56510.151	12.87
SWIFT J1515.0+4205	60061348002	56755.121	23.74
SWIFT J1519.6+6538	60061264002	56778.537	15.04
SWIFT J1530.0-1300	60160617002	57798.912	24.23
SWIFT J1533.2-0836	60061265002	57241.121	20.28
SWIFT J1535.9+5751	60061266002	56610.944	25.01
	60061266004	56623.195	20.70
SWIFT J1548.5-1344	60061267002	56897.201	21.18
SWIFT J1557.8-7913	60160627002	57581.457	16.10
SWIFT J1613.2-6043	60160632002	58235.480	22.05
SWIFT J1621.2+8104	60061270002	57012.240	29.07
SWIFT J1626.7+8530	60160639002	57912.081	26.41
SWIFT J1628.1+5145	60160640002	57153.654	23.70
SWIFT J1648.0-3037	60160648002	57846.308	17.48
SWIFT J1650.5+0434	60061273002	57790.725	21.03
SWIFT J1717.1-6249	60061277002	56348.898	17.04
	60261001002	57411.047	20.05
	60261001004	57624.369	22.29
SWIFT J1737.5-2908	60061279002	56916.577	20.29
SWIFT J1741.9-1211	60160670002	58043.261	21.37
SWIFT J1745.4+2906	60160674002	57000.228	20.30
SWIFT J1748.8-3257	60160677002	58531.657	21.80
SWIFT J1802.8-1455	60160680002	57509.424	19.88
SWIFT J1816.0+4236	60061283002	57197.664	11.72
	60061283004	57199.075	4.52
SWIFT J1824.2+1845	60160686002	57272.095	21.20
SWIFT J1824.3-5624	60061284002	56497.778	19.83
SWIFT J1826.8+3254	60061354002	56796.921	12.49
	60061354004	56798.390	8.76
SWIFT J1830.8+0928	60061285002	57341.950	22.72
SWIFT J1835.0+3240	60061286002	56188.630	16.63
	60001084002	56644.083	82.21
	60202015002	57629.545	22.79
	60202015004	57642.569	24.60
	60202015006	57653.512	20.38
	60202015008	57666.067	21.53
	60202015010	57678.152	20.85
SWIFT J1836.9-5924	60301028002	58004.736	74.61
SWIFT J1838.4-6524	60061288002	56347.893	22.14
	60301004002	58041.183	43.24
SWIFT J1842.0+7945	60001082002	56436.408	23.64
	60001082003	56436.827	37.81
SWIFT J1856.1+1539	60160701002	58039.371	18.16
SWIFT J1856.2-7829	60061290002	56500.494	17.97
SWIFT J1905.4+4231	60160705002	58160.115	16.24
SWIFT J1913.3-5010	60160706002	57094.259	24.14
SWIFT J1921.1-5842	60201042002	57584.694	92.09

Table 5: Continued.

Source Name	NuSTAR Obs ID	Obs date (MJD)	Exposure (ks)
SWIFT J1926.9+4140	60061334002	56798.593	21.35
SWIFT J1930.5+3414	60376001002	58036.289	50.32
SWIFT J1933.9+3258	60160714002	57539.642	12.65
SWIFT J1937.5-0613	60101003002	57296.750	65.02
SWIFT J1938.1-5108	60160716002	57584.225	21.83
SWIFT J1942.6-1024	60201028002	57573.751	143.12
SWIFT J1947.3+4447	60061292002	56237.349	18.21
SWIFT J1952.4+0237	60061293002	56437.760	19.81
SWIFT J2001.0-1811	60061295002	57686.346	21.32
SWIFT J2006.5+5619	60061355002	56838.959	21.37
SWIFT J2018.8+4041	60061297002	56647.520	20.81
SWIFT J2021.9+4400	60061298002	56933.670	21.10
SWIFT J2035.2+2604	60160741002	57541.659	12.56
SWIFT J2044.2-1045	60101043002	57141.602	165.50
	60101043004	57175.433	36.48
SWIFT J2052.0-5704	60061302002	56481.334	18.45
SWIFT J2114.4+8206	60061303002	57970.039	18.17
SWIFT J2118.9+3336	60061358002	57039.697	19.30
SWIFT J2127.4+5654	60001110002	56235.737	49.06
	60001110003	56236.755	28.49
	60001110005	56237.758	62.43
	60001110007	56239.711	42.11
SWIFT J2134.9-2729	60061306002	56587.268	19.81
	60363005002	57859.815	19.37
SWIFT J2200.9+1032	60160774002	57883.112	20.90
SWIFT J2201.9-3152	60061308002	56937.572	31.67
SWIFT J2209.4-4711	60001031002	56935.487	101.04
SWIFT J2211.7+1843	60301015002	58080.660	101.10
SWIFT J2223.9-0207	60160788002	57523.804	19.69
SWIFT J2235.9-2602	60201031002	57521.521	99.01
SWIFT J2236.7-1233	60002060002	56993.586	52.70
	60002060004	56998.292	47.89
	60002060006	57003.536	50.68
SWIFT J2240.2+0801	60061343002	56979.467	17.36
SWIFT J2246.0+3941	60261004002	57874.049	51.45
SWIFT J2301.4-5916	60160814002	58031.193	19.11
SWIFT J2303.3+0852	60101001002	57185.785	21.58
	60101001004	57350.693	20.03
	60101001006	57371.446	16.42
	60101001008	57378.430	18.98
	60101001010	57381.589	20.68
	60101001012	57383.064	19.23
	60101001014	57384.945	23.40
SWIFT J2304.8-0843	60201029002	57713.143	104.63
SWIFT J2325.5-3827	60160826002	57577.318	19.97
	80101001002	57915.198	76.50
SWIFT J2328.9+0328	60368002002	58032.135	21.22
SWIFT J2330.5+7124	60061320002	56956.670	16.08
SWIFT J2333.9-2342	60160832002	57233.017	20.79
SWIFT J2359.3-6058	60061330002	56879.728	22.57

Notes. The third column lists the start date of each observation.

Table 6: Best-fit parameters for all the sources.

Source Name	$N_H(10^{22}\text{cm}^{-2})$	Γ	R	Fe K α EW (eV)	E_c (keV)	χ^2/df
SWIFT J0001.6-7701	7.7 ± 2.0	1.88 ± 0.15	$0.89^{+0.66}_{-0.50}$	99^{+43}_{-46}	> 421	143.9/154
SWIFT J0005.0+7021	$8.6^{+1.7}_{-3.3}$	$1.81^{+0.19}_{-0.17}$	$0.30^{+0.65}_{-0.30}$	104^{+50}_{-41}	> 125	141.0/142
SWIFT J0010.5+1057	< 0.2	1.81 ± 0.03	$0.15^{+0.10}_{-0.08}$	32^{+12}_{-10}	> 442	774.2/801
SWIFT J0034.5-7904	$1.1^{+1.4}_{-1.1}$	$2.20^{+0.12}_{-0.13}$	$0.92^{+0.65}_{-0.51}$	120^{+34}_{-33}	> 234	213.0/209
SWIFT J0048.8+3155	10.9 ± 0.7	1.65 ± 0.05	$0.27^{+0.11}_{-0.10}$	58 ± 12	> 270	838.9/926
SWIFT J0051.9+1724	$0.7^{+1.1}_{-0.7}$	$1.86^{+0.06}_{-0.07}$	< 0.10	36^{+21}_{-19}	> 156	433.7/437
SWIFT J0100.9-4750	$3.5^{+1.3}_{-1.4}$	$1.71^{+0.03}_{-0.05}$	$0.04^{+0.09}_{-0.04}$	184^{+43}_{-34}	> 278	208.8/211
SWIFT J0105.6-3433	$3.3^{+1.9}_{-1.7}$	$1.66^{+0.14}_{-0.12}$	< 0.28	< 53	> 76	206.6/235
SWIFT J0114.5-3236	$28.7^{+3.7}_{-3.6}$	$1.73(f)$	$2.92^{+1.23}_{-0.88}$	128^{+53}_{-45}	144^{+180}_{-54}	121.6/141
SWIFT J0123.9-5846	< 0.3	1.94 ± 0.02	0.54 ± 0.08	156^{+10}_{-12}	> 560	1132.1/1137
SWIFT J0124.5+3350	7.2 ± 2.7	$1.50^{+0.16}_{-0.14}$	$0.19^{+0.38}_{-0.19}$	204^{+64}_{-60}	> 437	109.5/94
SWIFT J0128.0-1850	3.1 ± 1.1	2.11 ± 0.10	$1.29^{+0.52}_{-0.46}$	38^{+30}_{-23}	> 834	347.8/303
SWIFT J0140.6-5321	$5.5^{+1.3}_{-2.6}$	$1.88^{+0.03}_{-0.18}$	$0.50^{+0.64}_{-0.44}$	118^{+47}_{-43}	> 128	176.3/169
SWIFT J0152.8-0329	$18.6^{+3.0}_{-4.2}$	$1.78^{+0.13}_{-0.31}$	$2.22^{+1.68}_{-1.04}$	298^{+71}_{-66}	> 91	82.2/97
SWIFT J0155.4+0228	< 0.5	$1.72^{+0.09}_{-0.07}$	< 0.31	55^{+38}_{-34}	> 141	199.8/197
SWIFT J0206.2-0019	$0.2^{+1.9}_{-0.2}$	$1.74^{+0.18}_{-0.07}$	$0.84^{+0.74}_{-0.49}$	123^{+40}_{-34}	52^{+61}_{-17}	193.3/206
SWIFT J0214.6-0049	$0.3^{+1.5}_{-0.3}$	$1.65^{+0.13}_{-0.08}$	$0.27^{+0.35}_{-0.24}$	191^{+33}_{-30}	> 91	284.8/293
SWIFT J0214.9-6432	$0.7^{+1.5}_{-0.7}$	$1.77^{+0.09}_{-0.15}$	< 0.33	< 53	> 93	165.9/165
SWIFT J0226.4-2821	$0.4^{+2.3}_{-0.4}$	$1.88^{+0.21}_{-0.15}$	$1.10^{+1.25}_{-0.67}$	75^{+56}_{-46}	> 192	71.7/101
SWIFT J0228.1+3118	0.9 ± 0.3	1.92 ± 0.02	0.66 ± 0.09	138^{+13}_{-10}	> 2326	1192.5/1171
SWIFT J0230.2-0900	< 0.5	$2.14^{+0.07}_{-0.05}$	$1.21^{+0.45}_{-0.47}$	124^{+37}_{-30}	> 508	214.6/233
SWIFT J0234.6-0848	$7.1^{+1.2}_{-1.8}$	$2.12^{+0.08}_{-0.17}$	$1.90^{+1.03}_{-0.72}$	< 58	> 152	249.1/239
SWIFT J0235.3-2934	$1.6^{+2.3}_{-1.6}$	$1.81^{+0.09}_{-0.13}$	$0.23^{+0.26}_{-0.23}$	61^{+51}_{-46}	> 631	95.2/105
SWIFT J0241.3-0816	14.3 ± 1.2	$1.47^{+0.09}_{-0.08}$	$0.07^{+0.15}_{-0.07}$	156 ± 19	78^{+31}_{-18}	548.9/627
SWIFT J0241.6+0711	6.3 ± 1.7	$1.80^{+0.13}_{-0.16}$	$0.72^{+0.39}_{-0.53}$	341^{+78}_{-71}	> 445	83.8/80
SWIFT J0244.8+6227	< 0.3	1.75 ± 0.04	$0.64^{+0.19}_{-0.17}$	313^{+48}_{-42}	> 365	609.6/618
SWIFT J0308.5-7251	< 0.5	$2.03^{+0.08}_{-0.07}$	$0.91^{+0.47}_{-0.36}$	75^{+32}_{-35}	> 710	255.5/239
SWIFT J0318.7+6828	$9.4^{+3.2}_{-3.1}$	$1.59^{+0.21}_{-0.10}$	$0.15^{+0.43}_{-0.15}$	114^{+42}_{-46}	80^{+209}_{-35}	162.5/169
SWIFT J0324.8+3410	< 0.3	1.85 ± 0.03	$0.16^{+0.10}_{-0.09}$	34^{+13}_{-11}	> 1125	670.1/704
SWIFT J0325.0-4154	$1.4^{+2.0}_{-1.4}$	$2.13^{+0.14}_{-0.27}$	$1.94^{+2.80}_{-1.29}$	84^{+57}_{-60}	> 70	90.7/90
SWIFT J0347.0-3027	$0.8^{+3.5}_{-0.8}$	$1.61^{+0.13}_{-0.21}$	< 0.36	< 70	> 40	60.7/81
SWIFT J0356.9-4041	5.2 ± 2.5	1.70 ± 0.10	$0.13^{+0.17}_{-0.13}$	130^{+52}_{-48}	> 326	130.0/116
SWIFT J0418.3+3800	1.6 ± 0.4	1.75 ± 0.03	< 0.01	50 ± 8	231^{+125}_{-61}	1131.1/1055
SWIFT J0426.2-5711	0.6 ± 0.5	1.66 ± 0.04	0.31 ± 0.08	36^{+6}_{-8}	62^{+7}_{-6}	1122.4/1070
SWIFT J0433.0+0521	0.3 ± 0.2	1.85 ± 0.02	0.40 ± 0.05	55 ± 4	284^{+76}_{-51}	1669.2/1571
SWIFT J0437.4-4713	1.0 ± 0.6	2.18 ± 0.06	$1.35^{+0.27}_{-0.31}$	35^{+13}_{-15}	> 959	581.5/590
SWIFT J0441.2-2704	$1.2^{+1.4}_{-1.2}$	$2.10^{+0.06}_{-0.18}$	$1.05^{+1.03}_{-0.64}$	< 52	> 131	153.4/139
SWIFT J0456.3-7532	$1.4^{+0.8}_{-0.7}$	2.23 ± 0.08	$2.62^{+0.86}_{-0.66}$	72^{+25}_{-21}	> 1132	406.8/420
SWIFT J0501.9-3239	1.6 ± 0.6	1.66 ± 0.05	$0.65^{+0.15}_{-0.14}$	163^{+11}_{-13}	207^{+127}_{-59}	898.7/901
SWIFT J0504.6-7345	$1.4^{+4.1}_{-1.4}$	$1.61^{+0.44}_{-0.27}$	$1.94^{+4.02}_{-1.53}$	161^{+75}_{-65}	32^{+51}_{-12}	74.8/67
SWIFT J0505.8-2351	15.1 ± 1.4	1.77 ± 0.10	$0.55^{+0.27}_{-0.22}$	53^{+19}_{-23}	145^{+154}_{-51}	534.3/549
SWIFT J0508.1+1727	3.8 ± 1.4	$1.82^{+0.12}_{-0.11}$	$0.48^{+0.45}_{-0.33}$	120^{+37}_{-30}	> 325	250.9/240
SWIFT J0516.2-0009	< 0.2	1.84 ± 0.02	$0.49^{+0.10}_{-0.09}$	256^{+20}_{-23}	> 4161	948.6/926
	< 0.2	1.99 ± 0.02	0.56 ± 0.08	151^{+13}_{-14}	> 1631	1074.9/1086
SWIFT J0521.0-2522	8.4 ± 0.9	2.27 ± 0.07	$0.65^{+0.30}_{-0.24}$	362^{+44}_{-41}	> 742	591.5/589
SWIFT J0526.2-2118	$19.2^{+2.0}_{-2.1}$	$1.63^{+0.10}_{-0.13}$	$0.07^{+0.24}_{-0.07}$	35^{+34}_{-28}	> 137	295.9/284
SWIFT J0552.2-0727	5.1 ± 0.2	1.67 ± 0.01	< 0.01	39 ± 4	509^{+355}_{-149}	1537.0/1584
SWIFT J0554.8+4625	1.1 ± 0.3	1.90 ± 0.02	$0.42^{+0.07}_{-0.06}$	86 ± 6	> 565	1333.1/1314
SWIFT J0623.3-6438	$1.0^{+2.0}_{-1.0}$	$1.85^{+0.09}_{-0.11}$	$0.31^{+0.43}_{-0.30}$	< 55	> 280	176.7/185
SWIFT J0623.8-3215	< 0.5	$1.80^{+0.09}_{-0.07}$	$0.17^{+0.36}_{-0.17}$	< 52	> 265	145.3/155
SWIFT J0623.9-6058	$27.4^{+2.7}_{-3.2}$	$2.06^{+0.19}_{-0.26}$	$2.45^{+1.87}_{-1.11}$	< 60	> 86	149.4/178
SWIFT J0640.1-4328	$17.7^{+3.2}_{-3.0}$	$1.73(f)$	$0.63^{+0.36}_{-0.27}$	115^{+73}_{-59}	> 301	72.9/71
SWIFT J0641.3+3257	$16.0^{+2.1}_{-2.2}$	1.74 ± 0.13	$0.39^{+0.42}_{-0.32}$	64^{+45}_{-37}	> 458	171.2/192
SWIFT J0655.8+3957	< 1.7	$1.61^{+0.09}_{-0.16}$	< 0.23	97^{+69}_{-54}	> 112	86.5/83
SWIFT J0709.0-4642	$6.9^{+1.6}_{-2.6}$	$1.88^{+0.11}_{-0.21}$	$0.72^{+0.93}_{-0.57}$	< 73	> 130	147.6/155

Table 6: Continued.

Source Name	$N_H(10^{22}\text{cm}^{-2})$	Γ	R	Fe $K\alpha$ EW (eV)	E_c (keV)	χ^2/df
SWIFT J0714.3+4541	$0.9^{+1.1}_{-0.9}$	$2.11^{+0.12}_{-0.10}$	$2.39^{+0.91}_{-0.79}$	136^{+40}_{-45}	> 911	164.2/162
SWIFT J0736.9+5846	< 1.5	$1.84^{+0.15}_{-0.11}$	$1.37^{+0.96}_{-0.58}$	111 ± 58	> 744	115.9/112
SWIFT J0739.7-3142	$27.9^{+2.8}_{-2.7}$	$1.73(f)$	$1.86^{+0.64}_{-0.50}$	247^{+46}_{-49}	> 187	146.0/163
SWIFT J0742.3+8024	13.6 ± 3.9	$1.48^{+0.22}_{-0.23}$	< 0.32	< 34	51^{+97}_{-22}	113.2/115
SWIFT J0804.2+0507	$24.1^{+2.5}_{-2.4}$	1.65 ± 0.17	$1.33^{+0.69}_{-0.44}$	121^{+28}_{-36}	143^{+286}_{-60}	360.6/320
SWIFT J0804.6+1045	$14.6^{+2.2}_{-1.2}$	$1.83^{+0.13}_{-0.09}$	$0.02^{+0.32}_{-0.02}$	61^{+38}_{-40}	> 113	176.3/167
SWIFT J0810.9+7602	$0.2^{+1.6}_{-0.2}$	$2.04^{+0.13}_{-0.10}$	$1.50^{+0.85}_{-0.60}$	62^{+40}_{-39}	> 457	166.7/185
SWIFT J0823.4-0457	$25.3^{+1.5}_{-1.4}$	$1.73(f)$	$1.14^{+0.28}_{-0.24}$	36^{+29}_{-26}	> 290	280.3/320
SWIFT J0838.4-3557	$0.6^{+0.9}_{-0.6}$	2.05 ± 0.08	$1.03^{+0.40}_{-0.36}$	143^{+29}_{-28}	> 732	498.6/417
SWIFT J0843.5+3551	$35.5^{+3.0}_{-3.6}$	$1.81^{+0.24}_{-0.28}$	$0.82^{+0.29}_{-0.72}$	< 44	> 89	63.2/67
SWIFT J0855.6+6425	$13.7^{+2.5}_{-1.6}$	$1.94^{+0.18}_{-0.20}$	$1.75^{+0.74}_{-1.03}$	76^{+81}_{-74}	> 165	56.5/59
SWIFT J0856.0+7812	$26.6^{+1.6}_{-3.2}$	$1.73(f)$	$0.03^{+0.95}_{-0.03}$	231^{+96}_{-104}	> 58	60.5/53
SWIFT J0902.0+6007	$18.2^{+3.2}_{-4.5}$	$1.63^{+0.26}_{-0.15}$	$0.08^{+0.61}_{-0.08}$	175^{+96}_{-88}	> 147	60.0/45
SWIFT J0911.2+4533	40.1 ± 3.6	$1.73(f)$	$0.62^{+0.60}_{-0.44}$	< 76	105^{+246}_{-43}	93.7/95
SWIFT J0917.2-6221	2.0 ± 0.5	2.22 ± 0.05	$3.06^{+0.37}_{-0.33}$	32 ± 9	347^{+496}_{-132}	1030.5/933
SWIFT J0918.5+1618	$8.6^{+1.4}_{-1.5}$	$1.86^{+0.12}_{-0.13}$	$1.72^{+0.65}_{-0.49}$	154^{+25}_{-27}	> 165	345.3/327
SWIFT J0920.1+3712	$8.4^{+1.0}_{-1.9}$	$1.73^{+0.03}_{-0.14}$	$0.40^{+0.42}_{-0.35}$	148^{+39}_{-42}	> 177	218.2/189
SWIFT J0920.8-0805	8.8 ± 0.6	1.82 ± 0.05	$0.64^{+0.13}_{-0.12}$	84 ± 10	112^{+29}_{-19}	935.1/957
SWIFT J0923.7+2255	< 0.5	1.93 ± 0.04	0.49 ± 0.19	93^{+22}_{-23}	> 755	462.0/504
SWIFT J0925.0+5218	< 0.1	1.74 ± 0.01	0.04 ± 0.04	69^{+9}_{-7}	137^{+20}_{-15}	1421.4/1396
SWIFT J0925.2-8423	$0.4^{+1.8}_{-0.4}$	$1.83^{+0.16}_{-0.10}$	$1.21^{+0.70}_{-0.50}$	79^{+31}_{-29}	74^{+84}_{-20}	233.4/245
SWIFT J0926.1+6931	14.5 ± 1.9	1.86 ± 0.14	$0.67^{+0.60}_{-0.41}$	111^{+33}_{-31}	> 335	246.4/252
SWIFT J0945.6-1420	2.0 ± 0.4	1.80 ± 0.03	$0.15^{+0.09}_{-0.08}$	79 ± 10	> 3265	849.6/917
SWIFT J0947.6-3057	1.9 ± 0.3	1.91 ± 0.03	$1.11^{+0.12}_{-0.11}$	109^{+13}_{-10}	189^{+49}_{-33}	1228.6/1273
	1.9 ± 0.1	1.90 ± 0.01	0.90 ± 0.04	111^{+4}_{-5}	151^{+13}_{-11}	2178.7/2003
	1.3 ± 0.2	1.74 ± 0.01	0.60 ± 0.04	157 ± 6	113^{+8}_{-7}	2043.5/1997
	1.7 ± 0.2	1.81 ± 0.02	$0.61^{+0.06}_{-0.05}$	121 ± 8	152^{+20}_{-16}	1646.7/1653
	1.8 ± 0.1	1.78 ± 0.01	$0.58^{+0.04}_{-0.03}$	111^{+5}_{-4}	144^{+11}_{-10}	2179.1/2107
SWIFT J0947.7+0726	2.7 ± 1.3	1.64 ± 0.08	< 0.07	< 11	125^{+150}_{-48}	379.3/406
SWIFT J1021.7-0327	< 1.0	$1.81^{+0.09}_{-0.08}$	$0.75^{+0.51}_{-0.39}$	102 ± 39	158^{+144}_{-77}	208.7/209
SWIFT J1023.5+1952	2.0 ± 0.4	1.81 ± 0.04	$0.96^{+0.13}_{-0.12}$	100 ± 8	318^{+207}_{-93}	1196.8/1105
	1.9 ± 0.5	1.75 ± 0.05	$0.74^{+0.16}_{-0.14}$	151 ± 12	363^{+517}_{-140}	826.9/896
	1.7 ± 0.3	1.86 ± 0.03	$0.85^{+0.14}_{-0.13}$	101^{+9}_{-11}	> 2649	1035.2/967
	0.9 ± 0.3	1.85 ± 0.03	0.75 ± 0.11	97^{+8}_{-9}	> 3993	1092.9/1048
	1.2 ± 0.3	1.94 ± 0.03	$1.10^{+0.15}_{-0.14}$	56^{+9}_{-6}	> 2077	984.3/1057
	2.1 ± 0.4	1.88 ± 0.03	$0.84^{+0.15}_{-0.13}$	86^{+12}_{-9}	> 4007	903.8/940
	$5.7^{+0.2}_{-0.3}$	$1.96^{+0.01}_{-0.03}$	$1.25^{+0.13}_{-0.12}$	53 ± 7	> 1231	1242.0/1223
SWIFT J1043.4+1105	< 1.2	$1.60^{+0.11}_{-0.06}$	$0.11^{+0.38}_{-0.11}$	< 115	> 190	68.1/77
SWIFT J1044.1+7024	$17.8^{+2.3}_{-3.5}$	$1.76^{+0.14}_{-0.20}$	$0.67^{+0.80}_{-0.53}$	128^{+73}_{-61}	> 233	91.4/86
SWIFT J1044.8+3812	$5.7^{+2.3}_{-2.9}$	$1.57^{+0.06}_{-0.22}$	< 0.41	120^{+57}_{-62}	> 62	99.9/109
SWIFT J1046.8+2556	$10.5^{+4.9}_{-4.7}$	$1.41^{+0.35}_{-0.34}$	$0.47^{+0.97}_{-0.47}$	186^{+85}_{-88}	> 38	69.7/67
SWIFT J1049.4+2258	$39.6^{+4.6}_{-4.4}$	$1.44^{+0.15}_{-0.18}$	< 0.23	126^{+47}_{-49}	> 71	183.3/193
SWIFT J1052.8+1043	$7.7^{+2.2}_{-2.6}$	$1.51^{+0.15}_{-0.16}$	$0.06^{+0.33}_{-0.06}$	91^{+41}_{-37}	> 117	223.0/216
SWIFT J1059.8+6507	$5.4^{+4.2}_{-4.1}$	1.49 ± 0.29	$0.28^{+0.76}_{-0.28}$	148^{+68}_{-68}	51^{+198}_{-23}	71.4/86
SWIFT J1100.9+1104	$3.3^{+1.2}_{-1.9}$	$1.74^{+0.03}_{-0.12}$	$0.16^{+0.40}_{-0.16}$	102^{+43}_{-43}	> 174	130.6/140
SWIFT J1105.7+5854A	$18.1^{+3.4}_{-7.3}$	$1.88^{+0.25}_{-0.51}$	$1.90^{+4.22}_{-1.50}$	129^{+99}_{-87}	> 29	40.9/46
SWIFT J1106.5+7234	2.7 ± 0.3	1.74 ± 0.03	$0.69^{+0.11}_{-0.10}$	222^{+12}_{-11}	> 4940	1180.5/1100
SWIFT J1110.6-2832	< 1.2	$1.88^{+0.13}_{-0.10}$	$0.75^{+0.63}_{-0.42}$	< 27	> 305	75.2/115
SWIFT J1113.6+0936	< 1.1	$1.71^{+0.05}_{-0.02}$	< 0.10	78^{+36}_{-35}	> 481	306.9/258
SWIFT J1136.0+2132	< 1.1	$2.13^{+0.13}_{-0.11}$	$1.58^{+1.12}_{-0.67}$	60^{+48}_{-43}	> 758	114.2/111
SWIFT J1139.0-3743	$3.0^{+0.2}_{-0.3}$	$1.97^{+0.01}_{-0.03}$	$1.57^{+0.18}_{-0.13}$	90 ± 8	> 2289	1166.7/1080
	$4.3^{+0.4}_{-0.5}$	$1.98^{+0.02}_{-0.05}$	2.01 ± 0.25	111^{+12}_{-11}	> 776	1084.7/1042
	8.0 ± 0.5	1.98 ± 0.04	$2.42^{+0.38}_{-0.34}$	170 ± 16	> 2998	846.5/756
	6.5 ± 0.4	1.98 ± 0.03	$2.24^{+0.29}_{-0.26}$	133^{+13}_{-12}	> 3114	917.8/892
SWIFT J1139.1+5913	< 0.3	$1.78^{+0.07}_{-0.06}$	$0.54^{+0.34}_{-0.28}$	83^{+25}_{-23}	98^{+70}_{-30}	330.9/347

Table 6: Continued.

Source Name	$N_H(10^{22}\text{cm}^{-2})$	Γ	R	Fe $K\alpha$ EW (eV)	E_c (keV)	χ^2/df
SWIFT J1139.8+3157	$6.9^{+2.5}_{-4.5}$	$2.12^{+0.28}_{-0.40}$	$1.71^{+2.67}_{-1.33}$	< 155	> 50	34.2/39
SWIFT J1142.2+1021	< 0.9	$1.70^{+0.15}_{-0.12}$	$0.30^{+0.43}_{-0.30}$	161^{+73}_{-65}	> 88	77.7/75
SWIFT J1143.7+7942	$0.2^{+0.7}_{-0.2}$	$1.73^{+0.06}_{-0.04}$	$0.49^{+0.17}_{-0.15}$	67^{+16}_{-13}	266^{+458}_{-92}	712.7/708
SWIFT J1145.6-1819	$0.1^{+0.5}_{-0.1}$	$1.74^{+0.04}_{-0.02}$	$0.26^{+0.08}_{-0.07}$	96^{+15}_{-14}	112^{+24}_{-16}	1108.3/1083
SWIFT J1149.3-0414	< 0.6	$1.78^{+0.09}_{-0.07}$	$0.16^{+0.34}_{-0.16}$	171^{+47}_{-44}	> 208	126.1/158
SWIFT J1152.6-0512	$0.5^{+1.3}_{-0.5}$	$1.90^{+0.10}_{-0.09}$	$0.33^{+0.27}_{-0.27}$	< 24	> 511	175.7/206
SWIFT J1201.2-0341	$0.1^{+1.3}_{-0.1}$	$1.84^{+0.11}_{-0.07}$	$0.35^{+0.34}_{-0.24}$	49^{+31}_{-28}	> 327	264.0/244
SWIFT J1202.5+3332	4.5 ± 1.5	$1.47^{+0.13}_{-0.12}$	$0.40^{+0.25}_{-0.25}$	102^{+26}_{-29}	118^{+154}_{-44}	296.3/330
SWIFT J1205.8+4959	$0.7^{+1.7}_{-0.7}$	$2.14^{+0.17}_{-0.16}$	$2.28^{+1.65}_{-1.07}$	< 52	> 272	137.9/122
SWIFT J1207.5+3355	$5.7^{+1.4}_{-1.1}$	$1.81^{+0.04}_{-0.14}$	$0.43^{+0.53}_{-0.36}$	46^{+37}_{-45}	> 216	143.2/142
SWIFT J1210.1-4637	$1.4^{+1.5}_{-1.4}$	$1.99^{+0.21}_{-0.23}$	$1.26^{+1.17}_{-0.88}$	211^{+46}_{-71}	> 98	102.0/102
SWIFT J1210.5+3924	7.9 ± 0.3	1.70 ± 0.03	$1.01^{+0.09}_{-0.08}$	77 ± 6	132^{+17}_{-13}	1647.6/1604
	10.6 ± 0.2	1.54 ± 0.02	0.72 ± 0.05	111^{+5}_{-5}	99^{+6}_{-5}	2201.3/2138
	9.1 ± 0.2	1.59 ± 0.02	0.66 ± 0.04	94 ± 5	110^{+7}_{-6}	2410.7/2233
SWIFT J1217.2-2611	$12.5^{+1.5}_{-2.6}$	$1.86^{+0.12}_{-0.19}$	0.93 ± 0.62	< 15	> 198	158.4/175
SWIFT J1218.5+2952	0.8 ± 0.3	2.30 ± 0.03	$1.47^{+0.16}_{-0.17}$	40^{+7}_{-8}	> 2700	1004.8/936
SWIFT J1219.4+4720	11.4 ± 1.1	1.68 ± 0.09	$0.11^{+0.21}_{-0.11}$	67^{+22}_{-14}	68^{+40}_{-19}	560.8/567
SWIFT J1225.8+1240	37.6 ± 1.8	$1.73(f)$	$0.71^{+0.23}_{-0.11}$	293^{+30}_{-31}	> 455	476.0/397
SWIFT J1232.0-4802	$3.2^{+1.1}_{-1.2}$	$2.06^{+0.06}_{-0.07}$	$0.75^{+0.64}_{-0.49}$	71 ± 37	> 301	127.9/146
SWIFT J1232.1+2009	$1.3^{+2.0}_{-1.3}$	$2.27^{+0.31}_{-0.25}$	$2.25^{+4.17}_{-1.45}$	100^{+57}_{-59}	> 84	71.3/77
SWIFT J1239.3-1611	8.0 ± 3.2	1.79 ± 0.27	$0.85^{+1.24}_{-0.71}$	71^{+52}_{-48}	61^{+273}_{-30}	110.5/111
SWIFT J1239.6-0519	< 0.3	$1.81^{+0.02}_{-0.01}$	$0.49^{+0.09}_{-0.06}$	135 ± 8	> 6972	1232.0/1147
SWIFT J1241.6-5748	1.7 ± 0.7	1.82 ± 0.05	$0.23^{+0.16}_{-0.14}$	51^{+21}_{-15}	> 1826	531.6/593
SWIFT J1255.0-2657	$1.0^{+2.2}_{-1.0}$	1.59 ± 0.14	< 0.18	67^{+35}_{-44}	163^{+35}_{-103}	129.8/154
SWIFT J1315.8+4420	7.5 ± 1.2	1.76 ± 0.10	$0.99^{+0.29}_{-0.25}$	234^{+27}_{-33}	82^{+31}_{-18}	608.6/661
SWIFT J1325.4-4301	11.4 ± 0.1	1.73 ± 0.01	< 0.003	57 ± 2	272^{+24}_{-20}	2785.0/2689
SWIFT J1331.2-2524	< 0.5	$2.07^{+0.11}_{-0.08}$	$1.84^{+0.94}_{-0.64}$	161^{+36}_{-41}	> 735	191.0/202
SWIFT J1334.8-2328	9.1 ± 2.5	1.60 ± 0.19	$0.54^{+0.53}_{-0.38}$	138^{+38}_{-43}	90^{+181}_{-38}	158.6/173
SWIFT J1335.8-3416	$1.7^{+0.2}_{-0.1}$	$2.26^{+0.02}_{-0.01}$	$1.71^{+0.11}_{-0.09}$	84^{+7}_{-5}	> 12238	1724.3/1499
SWIFT J1338.2+0433	5.6 ± 1.2	1.66 ± 0.09	< 0.03	68^{+22}_{-25}	> 92	428.3/417
SWIFT J1341.5+6742	$15.9^{+1.6}_{-1.9}$	$2.03^{+0.03}_{-0.16}$	$1.70^{+1.30}_{-0.82}$	155^{+45}_{-41}	> 291	158.9/161
SWIFT J1341.9+3537	$3.9^{+0.5}_{-0.7}$	1.93 ± 0.06	$1.36^{+0.38}_{-0.32}$	82^{+18}_{-17}	> 1967	582.6/556
SWIFT J1347.4-6033	4.2 ± 0.3	$1.99^{+0.02}_{-0.03}$	1.04 ± 0.10	84^{+5}_{-6}	> 909	1500.6/1373
SWIFT J1349.3-3018	0.9 ± 0.2	1.75 ± 0.01	0.36 ± 0.03	84^{+4}_{-3}	276^{+45}_{-35}	2051.4/2012
SWIFT J1349.7+0209	3.0 ± 1.3	$1.89^{+0.14}_{-0.08}$	$0.77^{+0.65}_{-0.45}$	44 ± 35	> 373	198.0/195
SWIFT J1354.5+1326	$31.2^{+7.0}_{-7.2}$	$1.41^{+0.32}_{-0.30}$	$0.01^{+0.69}_{-0.01}$	< 63	107^{+553}_{-71}	51.9/70
SWIFT J1410.9-4229	$7.0^{+2.2}_{-2.4}$	$1.66^{+0.06}_{-0.18}$	$0.32^{+0.62}_{-0.32}$	62^{+55}_{-49}	> 253	105.3/94
SWIFT J1413.2-0312	3.9 ± 0.2	1.92 ± 0.02	$1.22^{+0.11}_{-0.09}$	121^{+8}_{-5}	> 8377	1384.2/1328
SWIFT J1417.9+2507	3.3 ± 0.6	1.68 ± 0.05	$0.29^{+0.11}_{-0.10}$	54^{+13}_{-10}	431^{+1150}_{-188}	942.3/887
	3.5 ± 0.6	1.81 ± 0.05	$0.62^{+0.14}_{-0.13}$	56^{+10}_{-12}	> 402	852.9/877
	4.1 ± 0.5	1.58 ± 0.04	0.40 ± 0.09	104^{+10}_{-9}	126^{+30}_{-21}	1088.2/1103
	1.8 ± 0.4	1.70 ± 0.04	$0.56^{+0.11}_{-0.10}$	93^{+10}_{-8}	150^{+43}_{-28}	1141.0/1095
	3.7 ± 0.5	1.51 ± 0.04	$0.45^{+0.10}_{-0.09}$	114^{+9}_{-10}	97^{+17}_{-13}	1039.4/1080
SWIFT J1427.5+1949	< 0.7	$2.03^{+0.09}_{-0.05}$	$0.89^{+0.43}_{-0.38}$	81^{+30}_{-33}	> 518	214.0/212
SWIFT J1429.2+0118	< 0.5	$2.26^{+0.08}_{-0.05}$	$2.75^{+0.99}_{-0.77}$	79^{+25}_{-24}	> 712	319.4/365
SWIFT J1433.9+0528	$7.6^{+1.7}_{-1.8}$	1.95 ± 0.16	$0.78^{+0.61}_{-0.49}$	117^{+37}_{-28}	> 94	224.7/223
SWIFT J1436.4+5846	$2.7^{+1.3}_{-1.2}$	$1.90^{+0.10}_{-0.09}$	$0.87^{+0.45}_{-0.34}$	98^{+39}_{-35}	> 1490	253.0/227
SWIFT J1441.4+5341	$25.4^{+1.7}_{-1.6}$	$1.73(f)$	$0.68^{+0.34}_{-0.29}$	62^{+38}_{-31}	174^{+357}_{-70}	265.6/259
SWIFT J1446.7-6416	$4.6^{+2.4}_{-2.3}$	$2.25^{+0.30}_{-0.25}$	$2.25^{+3.45}_{-1.39}$	56^{+56}_{-54}	> 167	91.5/87
SWIFT J1454.9-5133	< 0.7	$1.96^{+0.09}_{-0.08}$	$1.25^{+0.63}_{-0.45}$	103^{+36}_{-33}	> 920	226.6/211
SWIFT J1457.8-4308	$14.7^{+3.2}_{-3.9}$	$1.84^{+0.17}_{-0.32}$	$2.52^{+1.85}_{-1.24}$	89^{+52}_{-54}	> 83	83.8/96
SWIFT J1504.2+1025	$1.0^{+0.7}_{-0.7}$	$1.92^{+0.04}_{-0.10}$	$0.64^{+0.37}_{-0.23}$	73^{+25}_{-22}	> 319	399.5/433
SWIFT J1506.7+0353A	$0.5^{+1.7}_{-0.5}$	$2.01^{+0.16}_{-0.13}$	$1.31^{+1.02}_{-0.67}$	83^{+54}_{-50}	> 218	120.0/131
SWIFT J1506.7+0353B	$0.8^{+1.1}_{-0.8}$	$1.79^{+0.06}_{-0.09}$	< 0.12	39^{+27}_{-26}	> 220	302.0/310
SWIFT J1513.8-8125	$8.5^{+3.1}_{-3.2}$	$2.06^{+0.27}_{-0.28}$	$2.57^{+2.19}_{-1.26}$	< 33	> 42	74.8/89

Table 6: Continued.

Source Name	$N_H(10^{22}\text{cm}^{-2})$	Γ	R	Fe K α EW (eV)	E_c (keV)	χ^2/df
SWIFT J1515.0+4205	10.9 ± 1.0	$1.89^{+0.05}_{-0.07}$	$0.89^{+0.41}_{-0.37}$	113^{+34}_{-33}	> 705	282.7/248
SWIFT J1519.6+6538	$21.7^{+3.8}_{-3.7}$	$1.73(f)$	$0.98^{+0.55}_{-0.35}$	< 66	> 246	65.0/52
SWIFT J1530.0-1300	$2.0^{+1.8}_{-1.9}$	$1.90^{+0.13}_{-0.12}$	$0.57^{+0.40}_{-0.36}$	67^{+34}_{-36}	> 492	190.6/189
SWIFT J1533.2-0836	$5.8^{+1.1}_{-1.9}$	$1.67^{+0.03}_{-0.13}$	$0.34^{+0.55}_{-0.32}$	185^{+40}_{-53}	> 291	144.3/165
SWIFT J1535.9+5751	$0.4^{+1.1}_{-0.4}$	$1.72^{+0.10}_{-0.06}$	$0.60^{+0.30}_{-0.34}$	104^{+24}_{-25}	225^{+946}_{-105}	431.7/478
SWIFT J1548.5-1344	1.9 ± 0.8	$2.02^{+0.08}_{-0.07}$	$1.00^{+0.31}_{-0.26}$	139 ± 21	> 1393	456.7/458
SWIFT J1557.8-7913	$5.5^{+1.3}_{-2.5}$	$1.91^{+0.07}_{-0.11}$	$0.20^{+0.20}_{-0.43}$	< 24	> 569	173.2/169
SWIFT J1613.2-6043	1.7 ± 1.4	1.76 ± 0.13	$0.61^{+0.33}_{-0.29}$	139^{+28}_{-29}	> 88	349.1/316
SWIFT J1621.2+8104	$18.3^{+5.6}_{-5.4}$	$1.67^{+0.43}_{-0.40}$	$1.16^{+2.67}_{-1.06}$	211^{+66}_{-89}	44^{+226}_{-21}	66.6/71
SWIFT J1626.7+8530	< 0.9	$2.04^{+0.12}_{-0.06}$	$1.17^{+0.71}_{-0.42}$	119^{+38}_{-39}	> 635	185.7/196
SWIFT J1628.1+5145	19.8 ± 1.1	$1.73(f)$	$0.65^{+0.21}_{-0.19}$	50^{+20}_{-25}	206^{+201}_{-69}	400.6/404
SWIFT J1648.0-3037	< 1.6	1.70 ± 0.17	$0.09^{+1.46}_{-0.09}$	151^{+78}_{-85}	> 34	40.6/53
SWIFT J1650.5+0434	3.2 ± 1.5	$1.79^{+0.14}_{-0.13}$	$1.04^{+0.50}_{-0.39}$	55^{+29}_{-27}	> 98	263.6/315
SWIFT J1717.1-6249	$20.6^{+0.5}_{-0.4}$	1.90 ± 0.03	$1.42^{+0.16}_{-0.15}$	78 ± 9	> 6109	1107.0/1100
SWIFT J1737.5-2908	$3.1^{+0.6}_{-0.5}$	1.76 ± 0.05	$0.49^{+0.13}_{-0.12}$	29 ± 11	77^{+14}_{-11}	924.6/897
SWIFT J1741.9-1211	< 0.6	1.93 ± 0.07	$0.94^{+0.29}_{-0.30}$	230^{+62}_{-52}	> 826	346.2/342
SWIFT J1745.4+2906	$9.2^{+1.4}_{-2.4}$	$1.89^{+0.04}_{-0.09}$	$0.33^{+0.41}_{-0.33}$	< 64	> 193	183.8/201
SWIFT J1748.8-3257	$1.7^{+0.9}_{-1.0}$	$1.69^{+0.04}_{-0.07}$	< 0.09	81^{+27}_{-25}	> 172	312.6/329
SWIFT J1802.8-1455	$0.4^{+1.1}_{-0.4}$	$1.76^{+0.09}_{-0.06}$	$0.10^{+0.19}_{-0.10}$	254^{+33}_{-42}	> 138	578.6/535
SWIFT J1816.0+4236	$5.9^{+0.9}_{-1.5}$	$1.78^{+0.04}_{-0.09}$	$0.44^{+0.37}_{-0.28}$	59^{+26}_{-28}	> 306	282.7/262
SWIFT J1824.2+1845	$13.2^{+2.4}_{-3.9}$	$1.67^{+0.13}_{-0.26}$	$0.91^{+0.84}_{-0.57}$	143^{+55}_{-52}	> 97	95.4/118
SWIFT J1824.3-5624	$22.9^{+3.2}_{-3.1}$	1.65 ± 0.24	$2.17^{+1.33}_{-0.85}$	201^{+44}_{-42}	82^{+115}_{-31}	231.5/220
SWIFT J1826.8+3254	10.1 ± 1.4	1.77 ± 0.12	$0.48^{+0.32}_{-0.26}$	111^{+26}_{-20}	93^{+78}_{-30}	337.3/389
SWIFT J1830.8+0928	$20.2^{+2.7}_{-2.1}$	$1.77^{+0.14}_{-0.26}$	$0.17^{+0.68}_{-0.17}$	155^{+77}_{-64}	> 72	68.1/73
SWIFT J1835.0+3240	0.4 ± 0.3	1.73 ± 0.02	0.05 ± 0.04	66^{+7}_{-8}	234^{+60}_{-40}	1501.9/1565
SWIFT J1836.9-5924	$4.4^{+0.3}_{-0.4}$	$2.53^{+0.04}_{-0.03}$	$1.06^{+0.18}_{-0.19}$	62 ± 9	> 1454	836.6/775
SWIFT J1838.4-6524	22.9 ± 0.7	1.86 ± 0.05	$1.57^{+0.19}_{-0.17}$	112 ± 10	172^{+61}_{-36}	1230.3/1178
SWIFT J1842.0+7945	0.9 ± 0.4	1.75 ± 0.03	$0.18^{+0.07}_{-0.06}$	57^{+6}_{-9}	192^{+66}_{-40}	1144.6/1124
SWIFT J1856.1+1539	$6.8^{+1.1}_{-2.2}$	$1.96^{+0.05}_{-0.17}$	$1.04^{+0.68}_{-0.53}$	61^{+33}_{-31}	> 184	206.7/231
SWIFT J1856.2-7829	$2.3^{+1.0}_{-0.6}$	$2.13^{+0.09}_{-0.05}$	$1.65^{+0.79}_{-0.62}$	47^{+32}_{-31}	> 469	184.5/216
SWIFT J1905.4+4231	$1.6^{+2.0}_{-1.6}$	$1.82^{+0.12}_{-0.19}$	$0.22^{+0.65}_{-0.22}$	110^{+49}_{-50}	> 70	125.0/118
SWIFT J1913.3-5010	$24.5^{+3.8}_{-3.7}$	1.62 ± 0.22	$0.63^{+0.52}_{-0.38}$	66^{+43}_{-35}	> 79	152.7/189
SWIFT J1921.1-5842	< 1.6	$1.94^{+0.01}_{-0.02}$	$0.61^{+0.09}_{-0.06}$	124^{+15}_{-14}	> 1330	1059.3/1075
SWIFT J1926.9+4140	< 1.2	$1.83^{+0.16}_{-0.12}$	$0.47^{+0.81}_{-0.47}$	132^{+69}_{-81}	> 194	57.8/57
SWIFT J1930.5+3414	36.5 ± 2.9	$1.73(f)$	$2.24^{+0.63}_{-0.51}$	57^{+28}_{-33}	94^{+28}_{-18}	397.9/340
SWIFT J1933.9+3258	$1.0^{+1.1}_{-1.0}$	$2.25^{+0.09}_{-0.15}$	$2.39^{+1.37}_{-0.90}$	31^{+31}_{-25}	> 122	249.4/268
SWIFT J1937.5-0613	1.9 ± 0.4	2.48 ± 0.04	$1.32^{+0.25}_{-0.22}$	60^{+13}_{-9}	> 2212	751.4/742
SWIFT J1938.1-5108	$0.6^{+1.4}_{-0.6}$	$1.88^{+0.11}_{-0.09}$	$0.25^{+0.36}_{-0.25}$	68^{+33}_{-28}	> 265	249.2/246
SWIFT J1942.6-1024	0.9 ± 0.2	1.84 ± 0.02	0.56 ± 0.07	101^{+6}_{-5}	328^{+162}_{-83}	1459.3/1413
SWIFT J1947.3+4447	$11.6^{+1.7}_{-2.5}$	$1.83^{+0.06}_{-0.17}$	$0.29^{+0.45}_{-0.29}$	76^{+35}_{-32}	> 113	237.1/217
SWIFT J1952.4+0237	$34.6^{+3.2}_{-5.3}$	$1.71^{+0.09}_{-0.28}$	$0.49^{+0.69}_{-0.47}$	100^{+49}_{-43}	> 114	136.0/127
SWIFT J2001.0-1811	$5.8^{+0.7}_{-1.1}$	2.18 ± 0.09	$1.95^{+0.62}_{-0.52}$	33^{+25}_{-28}	> 659	305.4/278
SWIFT J2006.5+5619	$26.0^{+2.8}_{-4.2}$	$1.82^{+0.15}_{-0.21}$	$0.42^{+0.63}_{-0.24}$	< 93	> 175	71.1/75
SWIFT J2018.8+4041	$19.2^{+0.8}_{-2.9}$	$1.69^{+0.03}_{-0.18}$	$0.73^{+0.32}_{-0.39}$	125^{+32}_{-36}	> 193	194.4/214
SWIFT J2021.9+4400	$9.4^{+2.1}_{-3.5}$	$1.70^{+0.15}_{-0.28}$	$1.23^{+1.22}_{-0.80}$	161^{+60}_{-67}	> 101	99.9/100
SWIFT J2035.2+2604	< 2.8	$1.50^{+0.24}_{-0.15}$	$0.25^{+0.80}_{-0.25}$	83^{+58}_{-71}	56^{+199}_{-25}	65.5/67
SWIFT J2044.2-1045	< 0.02	1.75 ± 0.01	0.41 ± 0.04	69^{+6}_{-5}	106^{+7}_{-6}	1823.0/1637
SWIFT J2052.0-5704	25.4 ± 2.3	1.59 ± 0.15	$0.90^{+0.41}_{-0.32}$	198^{+28}_{-32}	108^{+98}_{-36}	373.0/391
SWIFT J2114.4+8206	$2.1^{+0.9}_{-1.6}$	$1.88^{+0.03}_{-0.12}$	$0.31^{+0.29}_{-0.23}$	67^{+27}_{-30}	> 220	341.7/349
SWIFT J2118.9+3336	$1.0^{+0.8}_{-1.0}$	$1.85^{+0.10}_{-0.11}$	$0.10^{+0.36}_{-0.10}$	91^{+26}_{-37}	> 110	286.1/248
SWIFT J2127.4+5654	0.9 ± 0.2	2.03 ± 0.03	$1.77^{+0.13}_{-0.12}$	58^{+5}_{-6}	102^{+12}_{-10}	1320.0/1348
SWIFT J2134.9-2729	1.5 ± 1.5	2.01 ± 0.13	$1.22^{+0.56}_{-0.43}$	105 ± 26	> 115	325.8/360
SWIFT J2200.9+1032	$0.4^{+1.3}_{-0.4}$	$1.57^{+0.11}_{-0.08}$	$0.39^{+0.30}_{-0.25}$	133^{+27}_{-28}	100^{+97}_{-33}	382.4/370
SWIFT J2201.9-3152	$12.6^{+0.3}_{-0.4}$	$1.89^{+0.01}_{-0.03}$	$0.62^{+0.10}_{-0.06}$	61^{+8}_{-9}	> 1100	1130.0/1102

Table 6: Continued.

Source Name	$N_H(10^{22}\text{cm}^{-2})$	Γ	R	Fe $K\alpha$ EW (eV)	E_c (keV)	χ^2/df
SWIFT J2209.4-4711	$1.2^{+0.4}_{-0.2}$	1.87 ± 0.04	< 0.06	84^{+14}_{-11}	340^{+165}_{-159}	832.7/883
SWIFT J2211.7+1843	$0.7^{+0.8}_{-0.7}$	1.93 ± 0.06	$0.41^{+0.18}_{-0.16}$	25^{+14}_{-12}	155^{+150}_{-53}	752.1/677
SWIFT J2223.9-0207	$21.1^{+1.8}_{-1.7}$	$1.73(f)$	$1.16^{+0.38}_{-0.32}$	64 ± 35	142^{+103}_{-43}	261.2/247
SWIFT J2235.9-2602	1.1 ± 0.2	$2.09^{+0.01}_{-0.02}$	$1.09^{+0.12}_{-0.11}$	170 ± 13	> 3190	1233.4/1222
SWIFT J2236.7-1233	$4.5^{+0.5}_{-0.8}$	1.87 ± 0.03	0.51 ± 0.19	90^{+19}_{-15}	> 1408	606.0/602
	2.5 ± 1.3	1.55 ± 0.10	< 0.22	140^{+23}_{-26}	172^{+689}_{-78}	473.4/446
	$6.7^{+1.4}_{-1.5}$	$1.73^{+0.08}_{-0.12}$	$0.29^{+0.29}_{-0.23}$	150^{+33}_{-23}	> 167	337.3/341
SWIFT J2240.2+0801	$2.7^{+2.0}_{-2.5}$	$1.97^{+0.16}_{-0.24}$	$1.55^{+1.33}_{-0.82}$	< 94	> 75	125.9/110
SWIFT J2246.0+3941	46.8 ± 2.3	$1.73(f)$	$0.69^{+0.22}_{-0.17}$	< 34	> 404	464.0/428
SWIFT J2301.4-5916	< 0.8	$1.73^{+0.09}_{-0.08}$	< 0.33	119^{+40}_{-38}	> 102	146.5/156
SWIFT J2303.3+0852	< 0.4	1.89 ± 0.01	$0.55^{+0.07}_{-0.06}$	131 ± 9	> 859	1412.4/1323
SWIFT J2304.8-0843	< 0.1	1.74 ± 0.01	0.10 ± 0.04	54 ± 5	222^{+46}_{-33}	1444.1/1447
SWIFT J2325.5-3827	2.0 ± 2.0	$1.96^{+0.21}_{-0.22}$	$0.93^{+1.24}_{-0.74}$	< 11	> 98	98.4/92
SWIFT J2328.9+0328	< 1.3	$2.03^{+0.19}_{-0.16}$	$2.02^{+1.99}_{-1.07}$	< 38	> 161	72.0/72
SWIFT J2330.5+7124	$7.7^{+4.7}_{-5.0}$	$1.73^{+0.30}_{-0.37}$	$0.78^{+1.37}_{-0.76}$	< 132	> 42	55.1/57
SWIFT J2333.9-2342	$1.4^{+0.8}_{-1.1}$	$1.93^{+0.05}_{-0.07}$	$0.04^{+0.20}_{-0.04}$	42^{+25}_{-29}	> 559	350.0/312
SWIFT J2359.3-6058	$12.5^{+4.3}_{-4.2}$	1.41 ± 0.27	$0.34^{+0.58}_{-0.34}$	189^{+58}_{-54}	57^{+121}_{-24}	100.9/114

Notes. The first column lists the Swift BAT name of the source. The next three columns list the best-fit results for the absorption, spectral index and reflection strength. The fifth column lists the Fe line equivalent width as estimated from the best-fit model and the sixth column lists the best-fit values of the high-energy cutoff. The last column lists the fit χ^2 statistic and the degrees of freedom. The error on equivalent width was estimated with N_H and R being fixed to their best-fit values and thus is only an underestimation of the real error. The values of 1.73(f) in the third column denote the sources that were fit with the power-law index fixed. The upper limits given in the second, fourth and fifth column and the lower limits in the sixth column correspond to 1- σ level.